Nuclear Engineering and Technology 58 (2026) 103887

Contents lists available at ScienceDirect

Nuclear Engineering and Technology

journal homepage: www.elsevier.com/locate/net

Original Article

Advanced Monte Carlo analysis of ex-vessel neutron dosimetry for cycle 25 of Krško nuclear power plant

Tanja Goričanec [a,b,*], Benjamin Barbarič [a], Vladimir Radulović [a,b], Dušan Čalič [a], Luka Snoj [a,b], Marjan Kromar [a]

[a] Jožef Stefan Institute, Jamova cesta 39, SI-1000, Ljubljana, Slovenia
[b] University of Ljubljana, Kongresni trg 12, SI-1000, Ljubljana, Slovenia

ARTICLE INFO

Keywords:
Krško nuclear power plant
MCNP
ADVANTG
Ex-vessel neutron dosimeters
Gradient chains

ABSTRACT

This paper presents the results of Monte Carlo neutron transport calculations performed for the containment building of the Krško Nuclear Power Plant. The calculations were performed using the Monte Carlo N-Particle Transport Code (MCNP) in combination with the ADVANTG hybrid code to speed up the convergence of the results outside the reactor core. The paper focuses on the analysis of the Ex-Vessel Neutron Dosimetry (EVND) program conducted during the 25^{th} fuel cycle at the Krško nuclear power plant with the irradiation of gradient chains and multiple foil sensor sets. The calculated reaction rates at the dosimeter locations are in good agreement with the measured values. However, deviations were observed in the thermal part of the neutron energy spectrum which cannot be neglected, and investigated were some possible reasons for the deviations: nuclear data, concrete material composition, concrete geometry, sensor position and impurities in sample.

1. Introduction

Numerous nuclear power plants (NPPs) around the world are approaching the end of their original design lifetime. In order to support life extension beyond these design limits, it is critical to evaluate reactor pressure vessel radiation embrittlement [1], as well as concrete degradation, swelling, corrosion, internal cracking, and other aspects [2]. Ensuring the safe long-term operation of these plants requires continuous monitoring of neutron irradiation and an assessment of the effects of neutron exposure on critical reactor components. Traditionally, in-vessel surveillance capsule dosimeters have been used to monitor pressure vessel neutron exposure. During plant lifetime, the in-vessel capsules are removed, examined and cannot be easily updated. The neutron monitors in these capsules undergo reactions with neutrons and provide experimental reaction rate values. However, the experimental data is limited to a relatively small portion of the phase space and does not provide detailed insight into the variability of neutron exposure across the azimuthal, axial and radial dimensions of the reactor vessel. To overcome these limitations, the ex-vessel dosimetry can be introduced to allow additional azimuthal and axial monitoring of neutron irradiation of the pressure vessel. By integrating the ex-vessel dosimetry program with the data from the in-vessel surveillance capsules, a plant-specific database can be created that facilitates the analysis of the vessel's neutron exposure and uncertainties throughout the operational history. A neutron measurement program outside the reactor vessel supports lifetime extension license renewal applications by delivering detailed data about the reactor vessel's neutron exposure. This system provides flexible monitoring of neutron flux gradients across the reactor vessel beltline (the area of the pressure vessel around the height of the core) and in areas important to reactor safety, enables continuous assessment of operational changes and fuel management impacts, and reduces uncertainties in exposure predictions through combined measurements and calculations [3,4].

In recent decades, significant progress has been made in calculation methods and experimental techniques used to evaluate the neutron fluence to reactor pressure vessel. Traditional neutron transport calculations were based on deterministic two-dimensional codes (e.g., DORT [5]) [6], but increasing emphasis has been placed on sophisticated Monte Carlo-based approaches (such as MCNP [7]) as they are able to accurately simulate complex geometries and physical interactions. However, accurate Monte Carlo-based evaluations require extensive computational resources and advanced variance reduction techniques to ensure statistical precision within reasonable computation times [8]. U.S. NRC Regulatory Guide 1.190 [9] explicitly recognizes the benefits of Monte Carlo simulations for the evaluation of

* Corresponding author at: Jožef Stefan Institute, Jamova cesta 39, SI-1000, Ljubljana, Slovenia.
E-mail address: tanja.goricanec@ijs.si (T. Goričanec).

https://doi.org/10.1016/j.net.2025.103887
Received 16 June 2025; Received in revised form 20 August 2025; Accepted 26 August 2025
Available online 1 September 2025

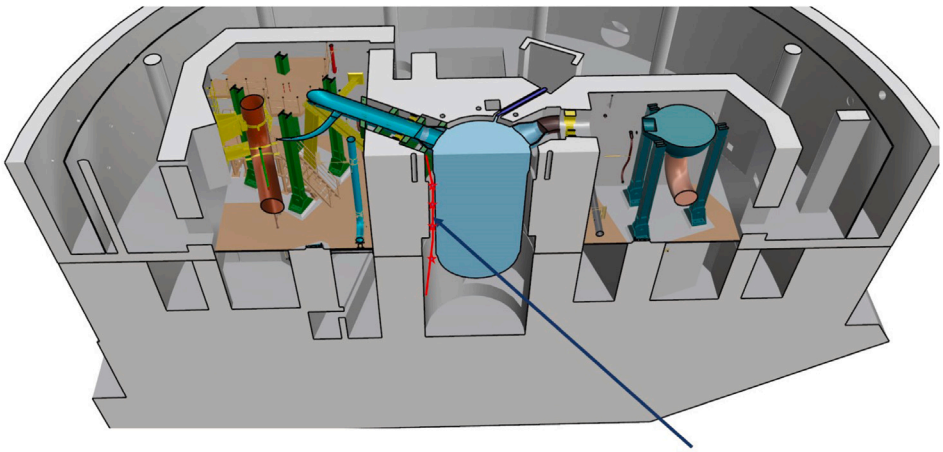

Fig. 1. Ex-vessel neutron dosimetry program in Krško NPP, schematic presentation of gradient chain location with surveillance capsules in CAD model of the containment.

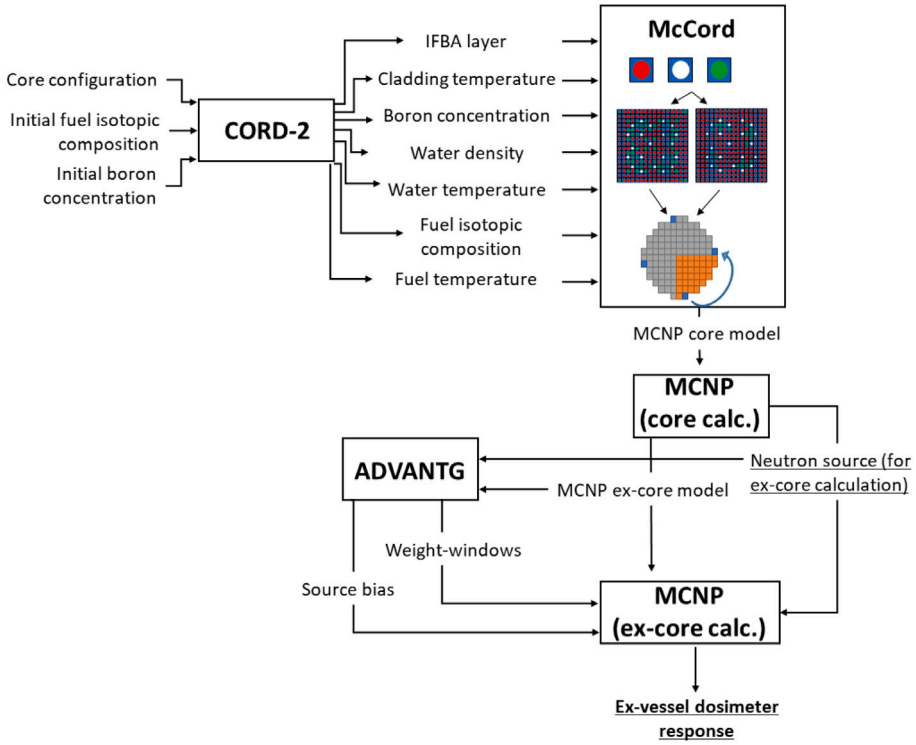

Fig. 2. Calculation procedure scheme to obtain ex-vessel neutron dosimeter response.

ex-vessel neutron dosimetry and provides comprehensive guidance on the modeling practices, statistical rigor, and validation requirements necessary for regulatory acceptance. In various studies, Monte Carlo methods have been successfully applied to benchmark fluence calculations [10,11], emphasizing the importance of careful consideration of geometric details, core neutron source description [9], nuclear cross-section uncertainties [12] and strategies to reduce variance in modeling, such as weight windows and source biasing techniques [13]. Despite their advantages, Monte Carlo simulations still face challenges related to computational cost, sensitivity to uncertainties in the input data, and the need for rigorous validation against experimental data, highlighting the ongoing need for research in this area.

A major challenge in ex-vessel neutron dosimetry (EVND) research is the limited public availability of detailed data from operating nuclear power plants, which often restricts open benchmarking and analysis. In this context, the present study offers a unique, open-science contribution: a state-of-the-art Monte Carlo analysis of the EVND program conducted during the 25th fuel cycle of the Krško NPP. The study is based on a high-fidelity MCNP model of the reactor core and containment, coupled with ADVANTG [14] for variance reduction, and employs detailed cycle- and burnup-specific neutron source terms to

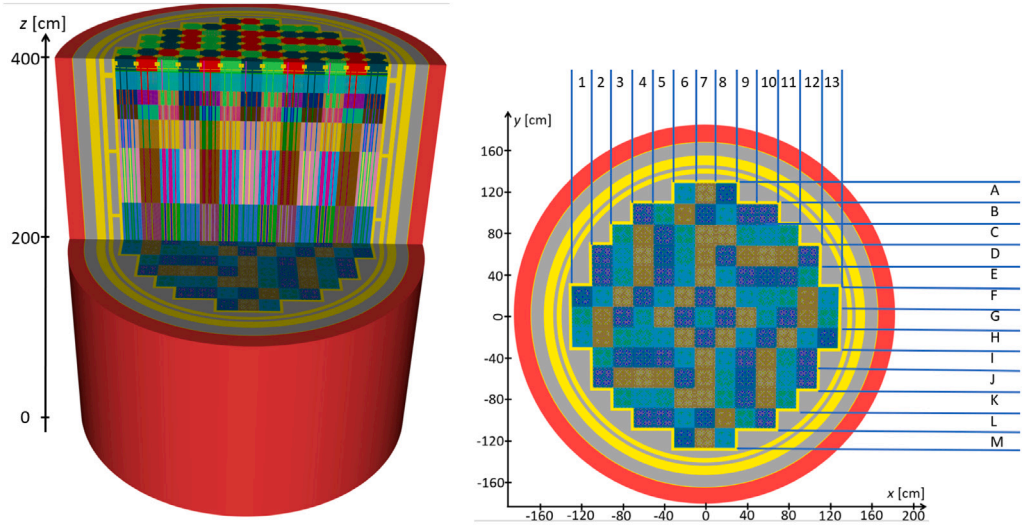

(a) 3D view. (b) xy view.

Fig. 3. MCNP reactor core model.

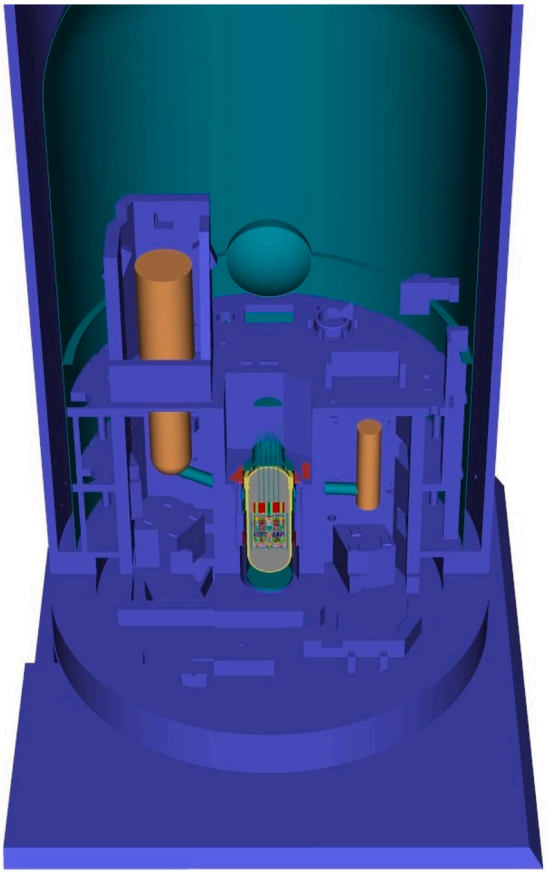

Fig. 4. 3D view of the geometry considered in the MCNP model of the Krško NPP containment building with reactor pressure vessel and surrounding concrete components. The figure was created using the Radiant utility within the ADVANTG suite [14].

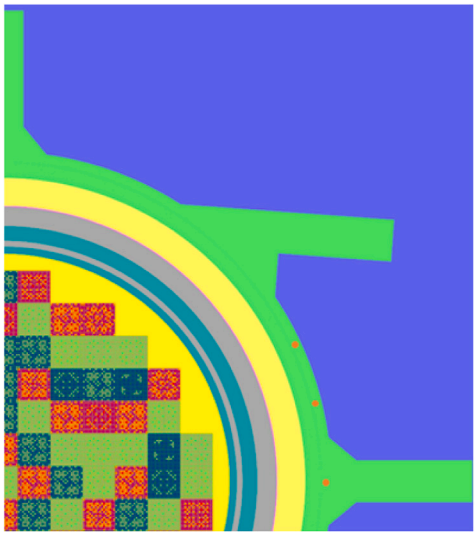

Fig. 5. Positions of EVND gradient chains in MCNP model. Only one quadrant is presented, however, calculations were performed with a full reactor core model.

accurately represent the operating conditions both at the beginning and at the end of cycle [15,16]. While Monte Carlo methods have been used in benchmark experiments (e.g. VENUS-3 [17]) or generic pressurized water reactor (PWR) models, there are only a few published studies applying them to EVND programmes for real plants with cycle-specific sources and fully detailed geometry [10]. In addition to comparing the simulations with the measured reaction rates, the study includes an extensive sensitivity analysis that addresses key uncertainty factors such as nuclear data, concrete material composition, geometry, dosimeter positioning and sample impurities. This work represents one of the most comprehensive and well documented EVND validation efforts using Monte Carlo methods in a commercial PWR environment.

The paper is structured as follows. Section 2 provides description of the ex-vessel neutron dosimetry program at Krško NPP. Section 3

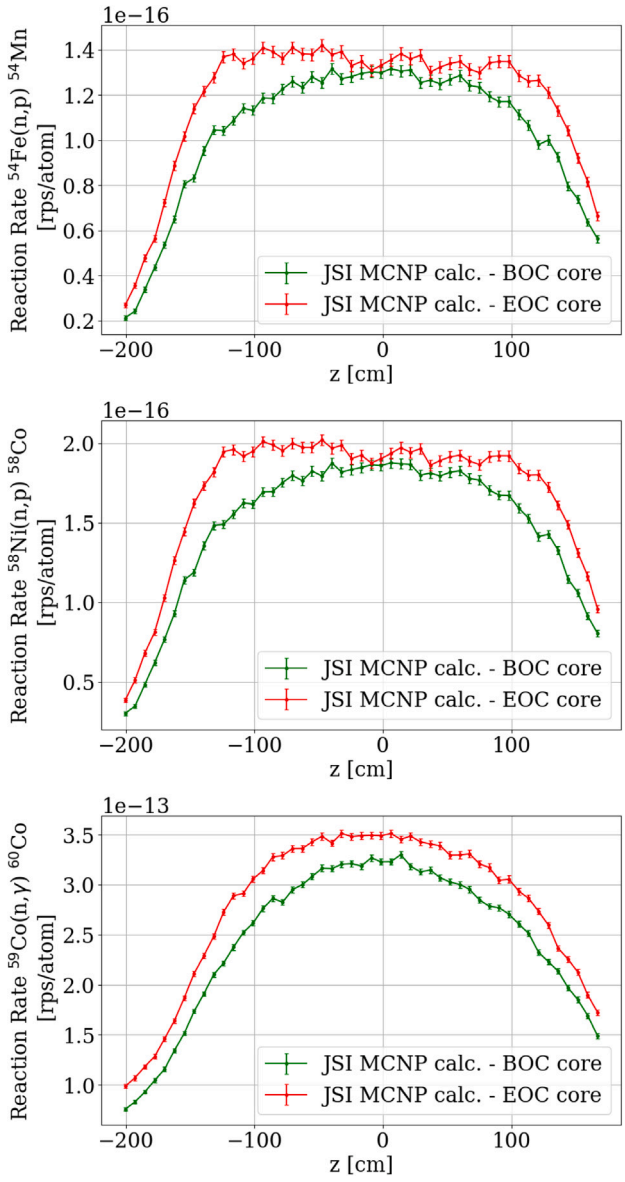

Fig. 6. Axial profiles of reaction rates at the beginning of the cycle (green) and at the end of the cycle (red) for the 25th fuel cycle in the Krško nuclear power plant for gradient chain at location 0°. The error bars represent 1 σ statistical uncertainties. The line connecting the data points serves as an eye guide only. (For interpretation of the references to color in this figure legend, the reader is referred to the web version of this article.)

presents the calculation methodology using MCNP models. Section 4 summarizes the calculation results and the sensitivity analysis. Section 5 provides concluding remarks. A detailed explanation about absolute normalization of MCNP calculation results is presented in Appendix A and the supplementary results in Appendix B The cross-sections for the reactions investigated as part of the EVND program are shown in Appendix C.

2. Ex-Vessel Neutron Dosimetry (EVND) at Krško NPP

Throughout Cycle 25 of the Krško Nuclear Power Plant (operational from October 25, 2010, to April 15, 2012), a novel Ex-Vessel Neutron Dosimetry (EVND) program was implemented to maintain real-time monitoring of neutron exposure within the reactor pressure vessel beltline. Integrating EVND with the extant surveillance capsule datasets creates a specific database for the plant, facilitating the assessment of neutron exposure to the vessel and related uncertainties for the duration of its operational life [3]. A significant aspect of this program is correlating neutron transport calculations with empirical data as described in the literature [10]. Historically, neutron transport calculations or normalized analytical results derived from internal surveillance capsules have been the industry's standards for predicting radiation effects on reactor vessels. Prior to the introduction of the EVND, Krško NPP utilized an in-vessel monitoring program, deploying six surveillance capsules on the thermal shield. Some of these capsules were periodically extracted for analysis.

The EVND program was initiated at the beginning of Krško NPP Cycle 25, focusing primarily on the continuous monitoring of activation in the reactor pressure vessel's beltline region. To achieve this, multiple sets of foil sensors (capsules) were strategically positioned at different points within the reactor cavity. Additionally, gradient chains accompanied the surveillance capsules to facilitate thorough azimuthal and axial neutron flux mapping of targeted areas. Upon the completion of cycle 25, new capsules were installed, and the previously irradiated capsules underwent analysis.

The dosimetry capsules contain activation monitors based on the following reactions: ^{63}Cu(n,α)^{60}Co, ^{54}Fe(n,p)^{54}Mn, ^{54}Fe(Cd)(n,p)^{54}Mn, ^{58}Ni(n,p)^{58}Co, ^{46}Ti(n,p)^{46}Sc, ^{93}Nb(n,n')^{93m}Nb, ^{59}Co(n,γ)^{60}Co, ^{59}Co(Cd)(n,γ)^{60}Co. Ex-vessel capsules were situated at three axial levels: centrally at the core's midplane and at two non-central locations (beneath the base of the active fuel and 20.3 cm beneath the top of the active fuel). These capsules were placed at three distinct azimuthal angles: 0°, 15°, and 30°. The two off-center positions were assessed only at an azimuthal angle of 0°. Measurement data were recorded in terms of disintegrations per second per gram (dps/g), with modified reaction rates provided as reactions per second per atom (rps/atom). Additionally, the stainless steel ex-vessel gradient chains, which facilitated the placement of the dosimetry capsules, contributed additional insights into the neutron fluence distribution spatially. The gradient chains measured 3 different reaction rates: ^{54}Fe(n,p)^{54}Mn, ^{58}Ni(n,p)^{58}Co and ^{59}Co(n,γ)^{60}Co. They were installed at azimuthal positions within the core quadrant corresponding to 0°, 15° and 30°. These assemblies were suspended within the annular cavity between the reactor pressure vessel and the surrounding biological shielding concrete, positioned at a radial distance of approximately 197.65 cm from the reactor core centerline (see Fig. 1). Measurements were conducted at 13 distinct axial locations, spanning a vertical range from approximately 170 cm to 200 cm relative to the core midplane.

3. Computational methods and models

This section presents the calculation procedure employed to obtain the response of the ex-vessel dosimeters (see Fig. 2). The methodology is based on Monte Carlo neutron transport simulations using MCNP [7], combined with variance reduction techniques to improve the accuracy of ex-vessel neutron flux calculations.

Two detailed computational models of the Krško NPP were developed in MCNP:

1. The MCNP core model, which accurately represents the reactor core configuration, including its temperature distributions, material densities, and isotopic compositions (Fig. 3).
2. The MCNP ex-core model, which includes the reactor pressure vessel (RPV), biological shielding, and other ex-core structures inside the containment building (Fig. 4)

Since fuel composition and operational parameters evolve over time, significant effort was invested in automating the generation of cycle-specific MCNP inputs. The core model used in this study has been extensively validated against:

- Deterministic neutron transport calculations preformed with the core design CORD-2 package [18]

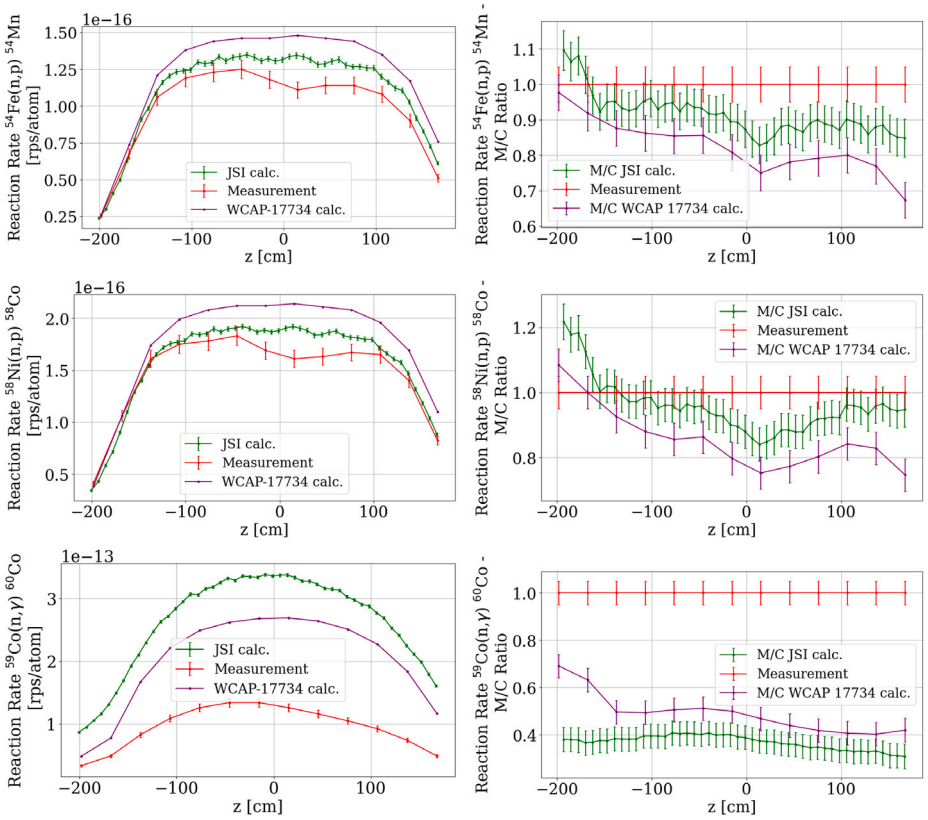

Fig. 7. Gradient chain at location 0° ^{54}Fe(n,p)^{54}Mn (top), ^{58}Ni(n,p)^{58}Co (middle) and ^{59}Co(n,γ)^{60}Co (bottom) reaction rate. The red color stands for measurements, the purple color for Westinghouse calculations [3] and the green color for MCNP calculations. The diagrams on the left show the axial profiles of the gradient chain and the diagrams on the right show the relative deviation of the different calculations from the measurement. The connecting lines serve as an eye guide only. The error bars represent 1 σ uncertainties. (For interpretation of the references to color in this figure legend, the reader is referred to the web version of this article.)

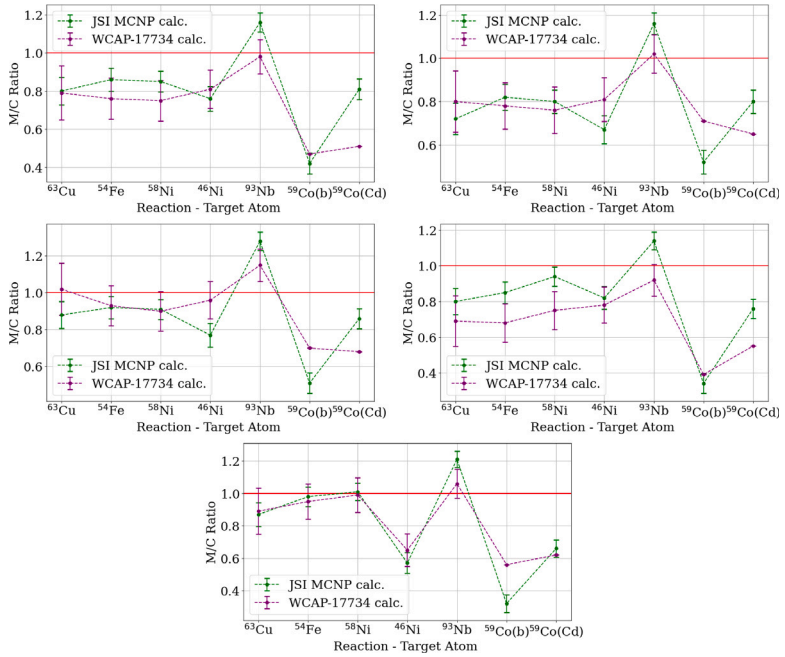

Fig. 8. Measured and calculated reaction rates at core midplane (0°, 15°, 30°), core top (0°) and core bottom (0°). Cycle 25. JSI results include both beginning-of-cycle and end-of-cycle core calculations.

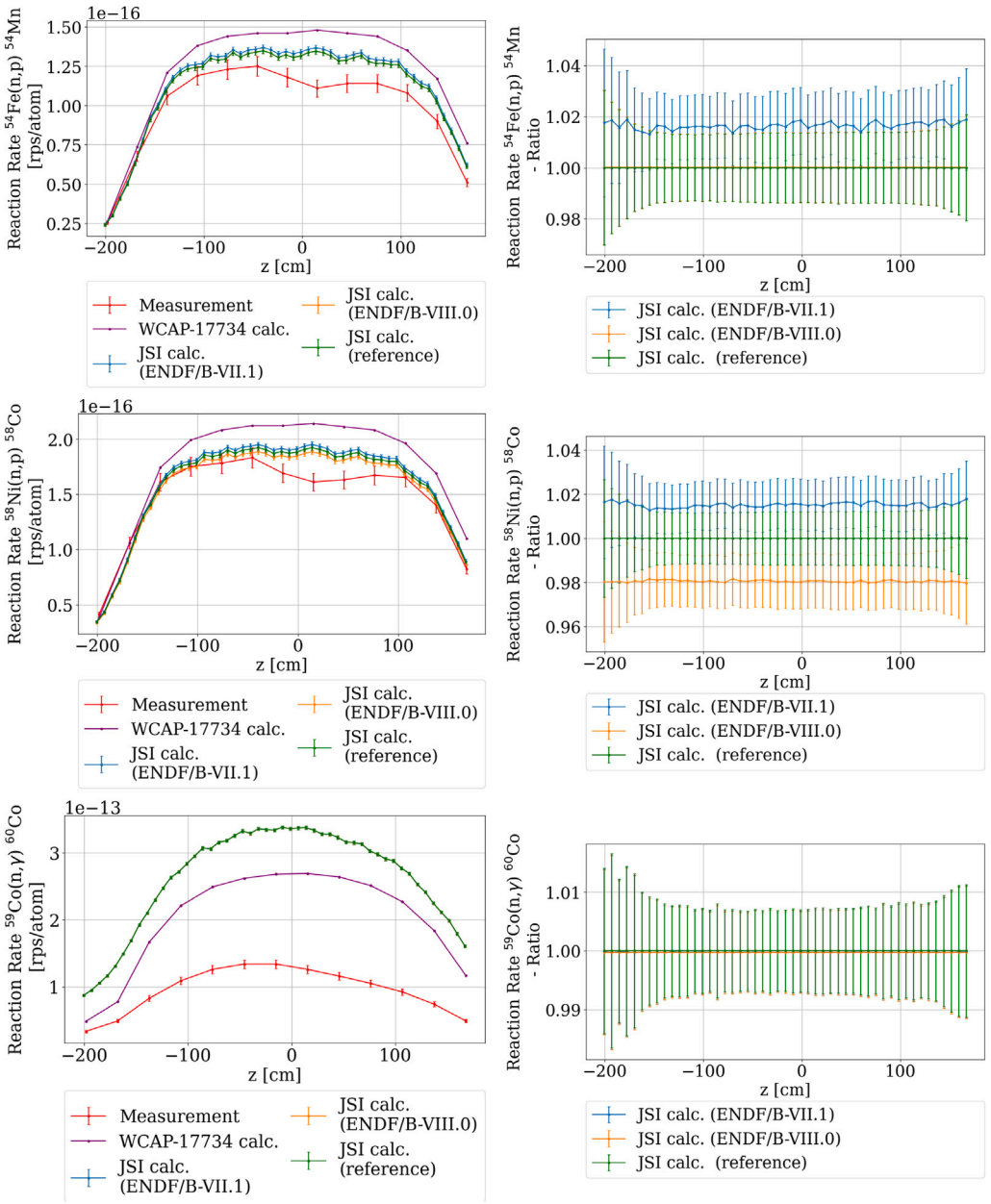

Fig. 9. Measured ^{54}Fe(n,p) (top), ^{58}Ni(n,p) (middle) and ^{59}Co(n,γ) (bottom) reaction rate in gradient chains sensitivity to nuclear data libraries at location 0°. Calculations with ENDF/B-VII.1 are shown in blue, calculations with ENDF/B-VIII.0 in orange and reference calculations with the IRDFF-II nuclear data library in green. The diagrams on the left show the axial profiles of the gradient chain and the diagrams on the right show the relative deviations of the different nuclear data libraries from the "reference source". The connecting lines serve as an eye guide only.

- In-core neutron detector measurements from the Krško NPP [19].

For this study, simulations were conducted for the Hot Full Power (HFP) core condition during the 25th fuel cycle. Two core burnup states were analyzed:

- Beginning of Cycle (BOC) – at 190 MWd/tU, representing a fresh fuel configuration.
- End of Cycle (EOC) – at 17,660 MWd/tU, representing a fully burned fuel core.

The MCNP core input serves as the basis for generating the neutron source term used in the MCNP ex-core model.

Because ex-vessel dosimeters are located outside the reactor core, far from the neutron source, direct Monte Carlo calculations are inefficient. To improve computational efficiency, a hybrid approach using the ADVANTG variance reduction code [14] was used to accelerate the convergence of the ex-vessel dosimeters response. To be able to use the ADVANTG code, the criticality-driven neutron source in the MCNP core model had to be converted to a fixed neutron source [20]. The effect of different descriptions of the fixed neutron source on the ex-core neutron transport calculations has been investigated in previous research [16], emphasizing the importance of the detailed geometry and description of the prompt fission neutron spectrum.

For the work presented in this paper, the ADVANTG code version 3.2.1 [14] was used to accelerate the convergence of the response of the ex-core neutron detectors using weight windows and source bias. The weight window technique is used to individually optimize the response calculations in ex-vessel dosimeters or ex-vessel gradient chains. Variance reduction parameters were generated using the *bplus* multigroup nuclear data library, which includes up-scattering and the

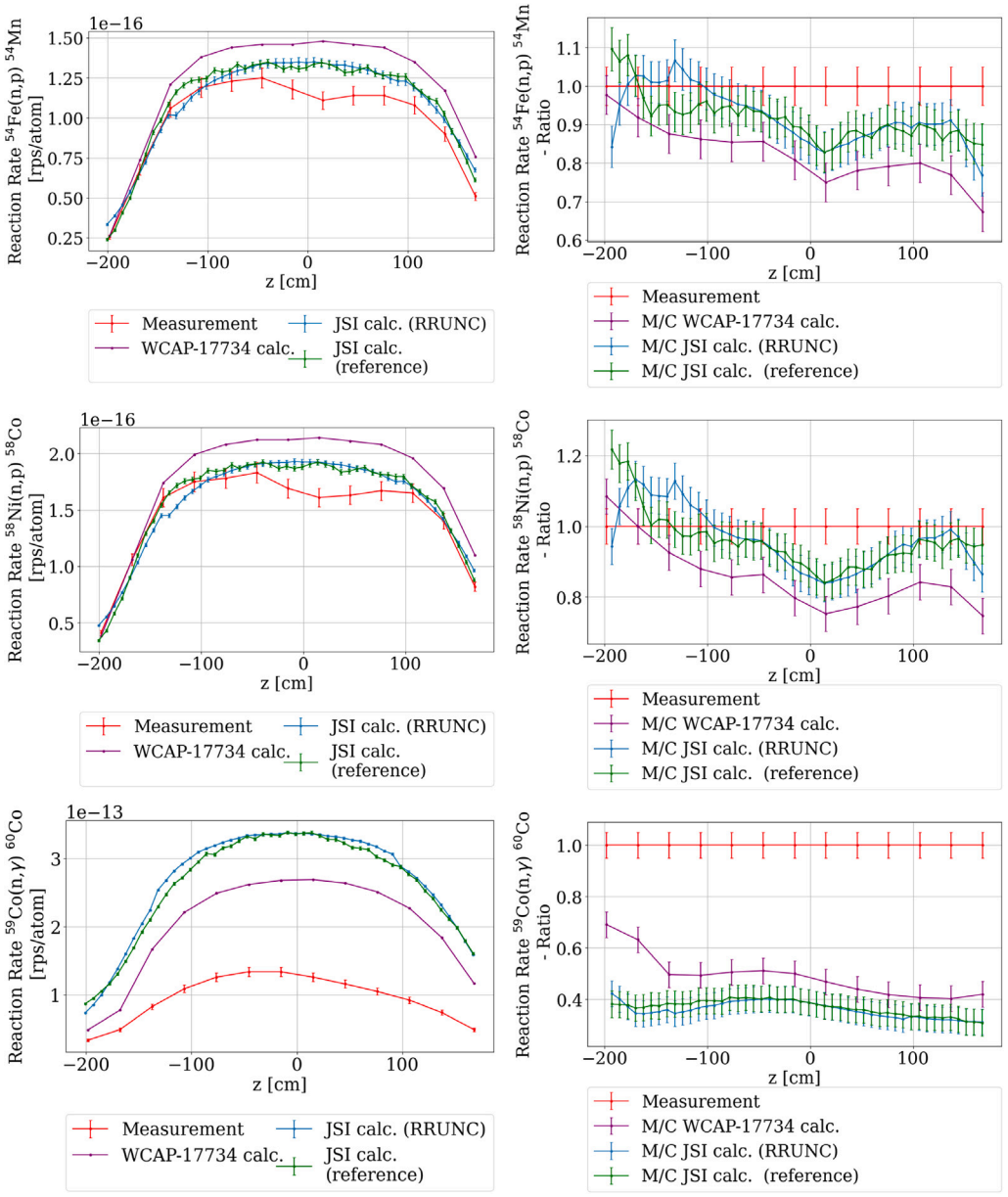

Fig. 10. Measured ^{54}Fe(n,p), ^{58}Ni(n,p), and ^{59}Co(n,γ) reaction rates in gradient chains at location 0° compared to MCNP and RR_UNC tool calculation. The uncertainties in RR_UNC calculation include both statistical and cross section data uncertainty. The diagrams on the left show the axial profiles of the gradient chain and the diagrams on the right show the relative deviations between the different axial positions. The connecting lines serve as an eye guide only.

FW-CADIS methodology [14] covering the reactor core and ex-core dosimeters. Default values were used for other solver options. To ensure that the final results were valid and the convergence criteria were met, statistical tests were checked in the MCNP output file.

4. Results

This section presents the results of neutron transport simulations performed for the Krško NPP using MCNP and ADVANTG, with a focus on the response of ex-vessel dosimeters and gradient chains. The results include normalization parameters used for obtaining absolute reaction rates, comparisons of calculated and measured dosimetry data, and sensitivity analyses investigating key uncertainties. The evaluation of uncertainties connected to measurements (e.g. measurement location) and the effect of different nuclear data libraries are discussed in detail. Additionally, potential sources of discrepancies between simulations and measurements, such as variations in concrete composition, geometric effects, and positioning uncertainties, are analyzed.

All results presented in this paper were calculated using MCNP version 6.1.1 [7] in conjunction with the ENDF/B-VIII.0 nuclear data library [21]. The nuclear data library used for the calculations of the reaction rates in the dosimeters was IRDFF-II [22]. Dataset including calculation results presented in this paper is published in Ref. [23].

To obtain the absolute normalized values, a normalization factor (K) must be applied [24]. In the case that the reactor is operating with a constant thermal power P, the coefficient K is determined by the average deposited energy per fission w_f, the average number of neutrons produced per fission $\overline{\nu}$, and the effective multiplication factor of the system k_{eff}. The normalization coefficient is expressed as follows:

$$K = \frac{P\overline{\nu}}{w_f k_{eff}}. \tag{1}$$

This assumption applies to systems close to criticality or when $k_{eff} \sim 1$ [24]. A detailed description about absolute normalization of the data presented in this paper is explained in Appendix A.

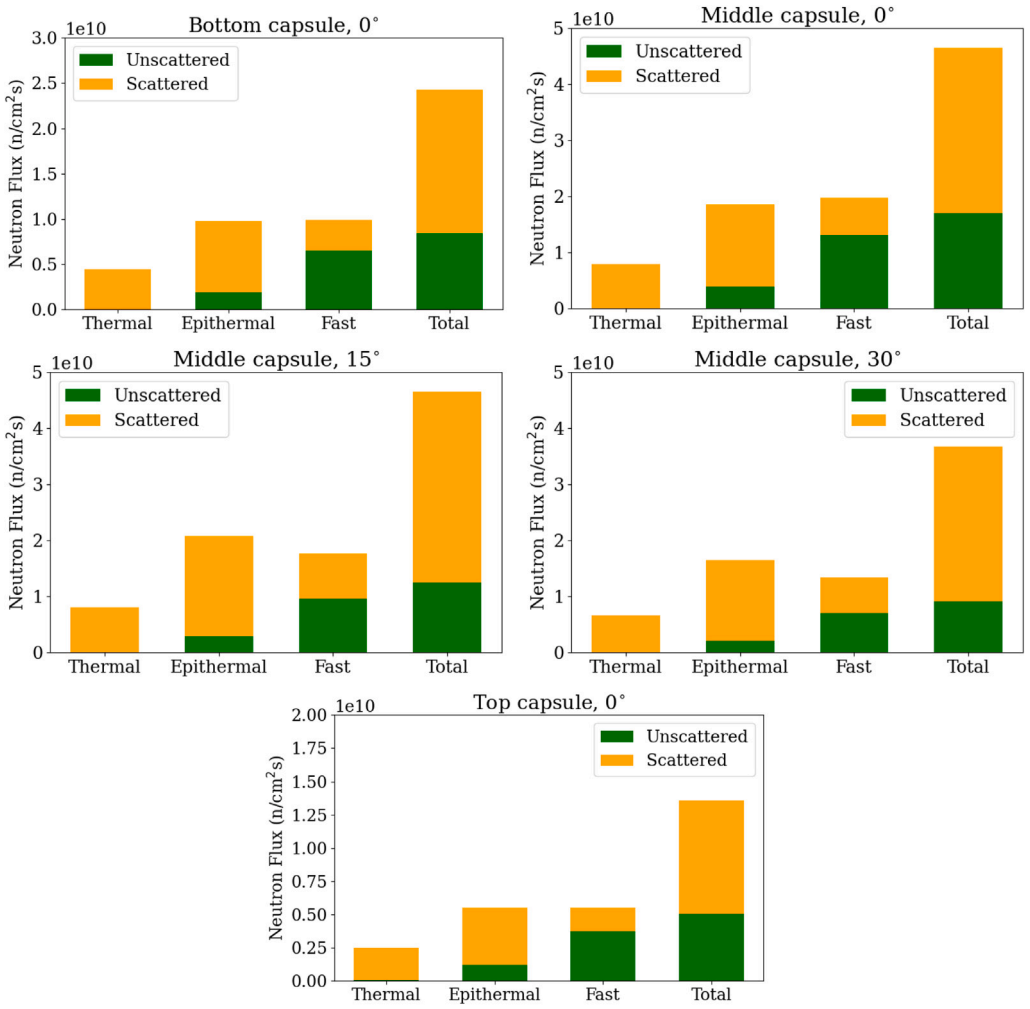

Fig. 11. Neutron flux in 3 energy groups with marked fraction of the total neutron flux due to neutrons originating from the surrounding concrete and backscattered into the EVND locations.

4.1. Reaction rates in gradient chains

This section deals with the evaluation of the reaction rates in gradient chains in the reactor cavity. Three sets of gradient chains were positioned at azimuthal positions corresponding to 0°, 15° and 30° in a core quadrant, as shown in Fig. 5. The dosimeter sets are suspended in the annular gap between the reflective insulation of the reactor pressure vessel and the concrete biological shielding at a radial distance of approximately 197.65 cm relative to the centerline of the reactor core [3]. At all three azimuthal locations, the stainless steel gradient chains are extended by about 2 m above and below the core center midplane of the active core height [3]. These segments allow measurements of the following reaction rates: ^{54}Fe(n,p)^{54}Mn, ^{58}Ni(n,p)^{58}Co and ^{59}Co(n,γ)^{60}Co, and are used to complete the determination of the axial and azimuthal gradients. Due to their small volume, gradient chains were not explicitly modeled in the Monte Carlo simulations. Instead, the reaction rates for the individual isotopes were estimated by performing the calculations across 50 discrete axial segments, each located at a fixed radial distance of 197.65 cm from the reactor core centerline (equivalent to 13.17 cm from the reactor pressure vessel). These axial segments spanned from −213.98 cm to 168.78 cm, relative to the core midplane, defined as the axial position $z = 0$ cm, which corresponds to the center of the active fuel height.

The results of the EVND gradient chain calculations were obtained for all three azimuthal locations and subsequently averaged across all four core quadrants, accounting for the inherent symmetry of the reactor core. This quadrant-wise averaging was employed to enhance statistical reliability and to mitigate potential discrepancies among quadrants that may arise from convergence issues in the Monte Carlo simulations [19]. Given the symmetrical core configuration, no significant asymmetry in the computational results is anticipated. Fig. 6 illustrates a comparison of the calculated axial reaction rate profiles at the beginning (BOC) and end (EOC) of the fuel cycle. As expected, the axial distribution of reaction rates evolves throughout the cycle, reflecting changes in core power distribution and fuel isotopic composition. To obtain a representative measure for the 25th fuel cycle, the cycle-averaged reaction rates were derived by averaging the BOC and EOC results.

The results at 0° azimuthal location are presented in Fig. 7, while the supplementary results for other azimuthal positions were moved to Appendix B for the better readability of the manuscript. In the MCNP simulations, the error bars indicate one standard deviation (1σ) statistical uncertainties. The uncertainties associated with the Westinghouse calculations were adopted from the report cited in [3], while measurement uncertainties were assumed to be 5%, consistent with the assumptions reported in the same reference.

The absolute comparison of calculations and dosimetry measurements is considered to be relatively difficult (see Ref. [25], page 122). It is observed that the calculated reaction rates agree with the measured values within ~15% for the ^{54}Fe and ^{58}Ni gradient chain. According to Regulatory Guide 1.190 [9] states that calculated reaction rates typically agree with the measurements within 30% for cavity dosimetry.

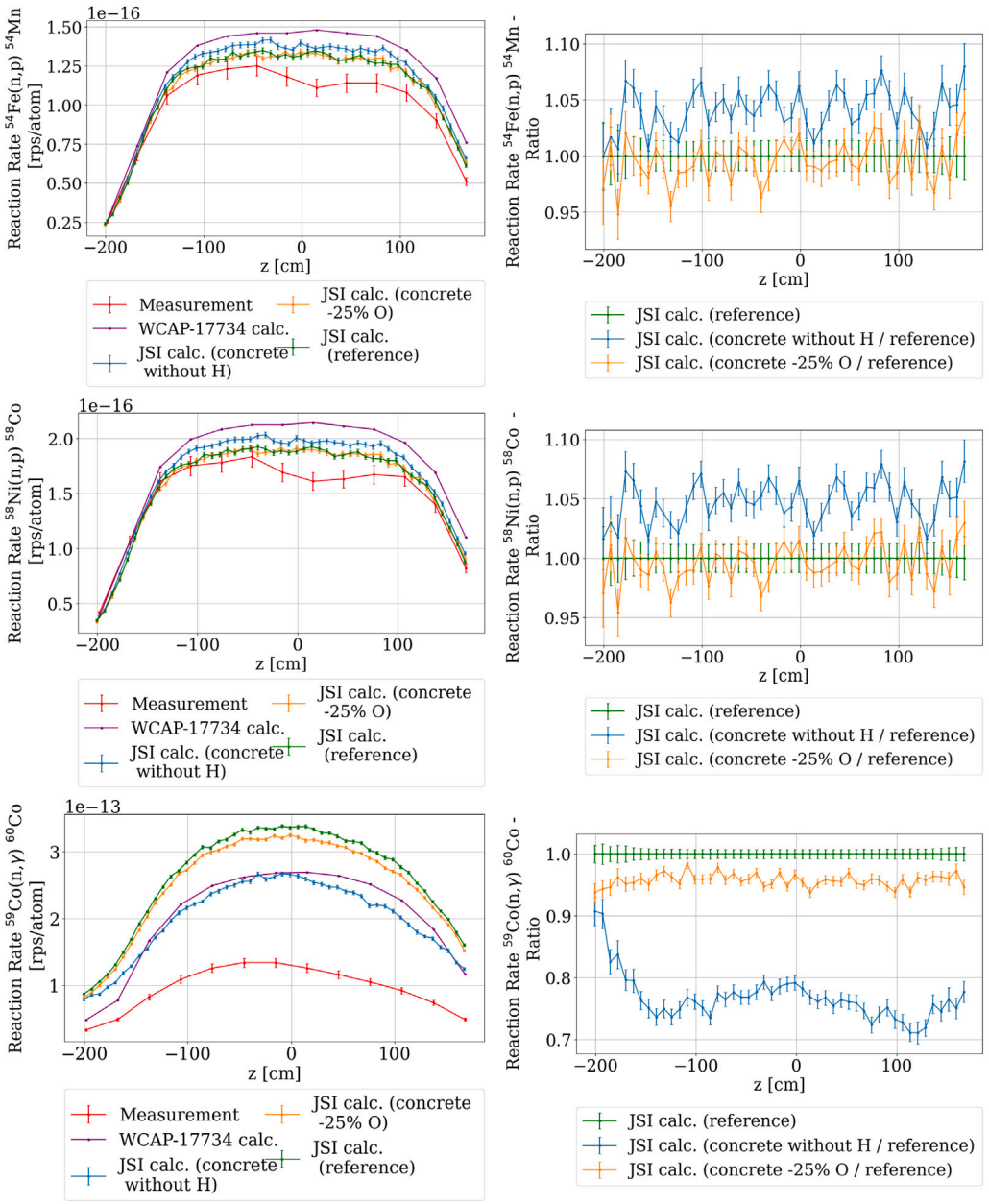

Fig. 12. Measured ^{54}Fe(n,p) (top), ^{58}Ni(n,p) (middle) and ^{59}Co(n,γ) (bottom) reaction rates in gradient chains sensitivity to water content in surrounding concrete at location 0° (top), 15° (middle) and 30° (bottom). Calculations without hydrogen in the concrete surrounding reactor pressure vessel are marked in blue, with reduced oxygen for ~25% in yellow, reference calculations with reference concrete composition are marked in green. The diagrams on the left show the axial profiles of the gradient chains and the diagrams on the right show the relative deviation between the different concrete compositions. The connecting lines serve as an eye guide only. (For interpretation of the references to color in this figure legend, the reader is referred to the web version of this article.)

Furthermore, the MCNP-based results presented in this study exhibit better overall agreement with experimental data compared to those obtained using the Westinghouse methodology, as reported in [3].

Notably, significant discrepancies – up to 70% – are observed for the ^{59}Co gradient chain results. However, these deviations are not considered representative due to the strong sensitivity of the ^{59}Co(n,γ) reaction to thermal neutrons. In contrast, ^{54}Fe and ^{58}Ni activation reactions are sensitive primarily to fast neutrons, with threshold energies exceeding 1 MeV (see Appendix C). A dedicated sensitivity analysis was conducted to investigate potential contributors to the observed discrepancies in the ^{59}Co results. Factors considered include sensitivities to nuclear data uncertainties, variations in concrete composition, the presence of structural cracking, dosimeter positioning inaccuracies, and the influence of trace impurities.

4.2. Reaction rates in EVND capsules

In addition to the gradient chains, ex-vessel neutron dosimeter sets were installed outside the vessel in the Krško NPP during the 25th fuel cycle. The energy dependence of the individual reaction cross sections (see Appendix C) shows that most of the reactions are threshold reactions with threshold energies >0.1 MeV. The cut-off energy of cadmium is 0.55 eV, well below the threshold energy of the observed reactions (apart from ^{59}Co(n,γ)^{60}Co), so it can be concluded that Cd has a negligible effect on these reactions. When analyzing the individual foils, their positioning within the sensor set was taken into account and the sensor set was explicitly added to the MCNP model. The comparison of the neutron spectrum between BOC and EOC is shown in Fig. 24, where minimal deviations between both spectra can be observed. The

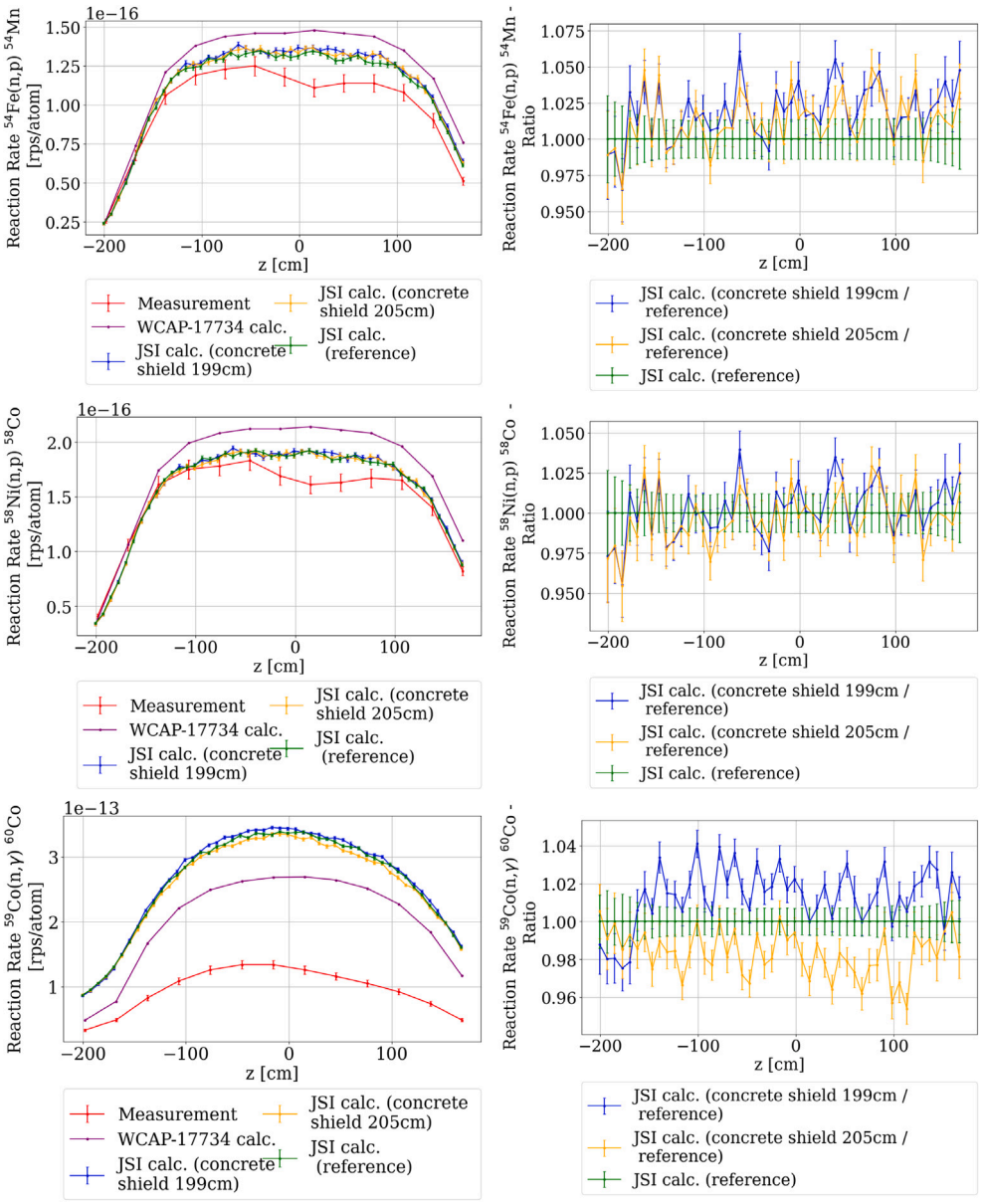

Fig. 13. Measured ^{54}Fe(n,p) (top), ^{58}Ni(n,p) (middle) and ^{59}Co(n,γ) (bottom) reaction rates in gradient chains sensitivity to surrounding concrete radius at location 0° (top). Calculations with a smaller concrete radius (199 cm) are marked in blue, calculations with a larger concrete radius (205.6 cm) are marked in orange, reference calculations with a reference concrete radius (200.6 cm) are marked in green. The diagrams on the left show the axial profiles of the gradient chain and the diagrams on the right show the relative deviations between the different concrete geometries. The connecting lines serve as an eye guide only. (For interpretation of the references to color in this figure legend, the reader is referred to the web version of this article.)

averaged results between BOC and EOC core configuration are shown in Appendix B. The reaction rates were calculated as an average between equivalent azimuthal positions in all 4 quadrants. The agreement of the reaction rates calculated with MCNP with the measurements is comparable to the Westinghouse calculations listed in the Ref. [3]. The summarized results for EVND capsules are presented in Fig. 8 Similarly to the gradient chains, the calculated ^{59}Co(n,γ)^{60}Co reaction rates without cadmium filter do not agree well with the measurements. The magnitude of the observed deviations in this work is typical in such evaluations (see Ref. [25], page 122).

4.3. Sensitivity studies

In this section, a thorough sensitivity study of the EVND gradient chains was performed, including sensitivities related to: nuclear data, concrete material composition, concrete geometry, position and impurities. Each of the assessed uncertainties is presented in a separate subsection.

4.3.1. Sensitivity to nuclear data

The effect of the nuclear data libraries on the calculated EVND results was investigated by changing the nuclear data library used to calculate the reaction rates of the individual gradient chains. The nuclear data libraries studied were: ENDF/B-VII.1 [26], ENDF/B-VIII.0 [21] and IRDFF-II [22]. For the reference results presented in this report, the IRDFF-II nuclear data library was used, which is specialized for use in dosimetry calculations. The results for azimuthal position at 0° are shown in Fig. 9, while the results for other azimuthal positions are presented in Appendix B. It can be observed that the deviations are within the uncertainties.

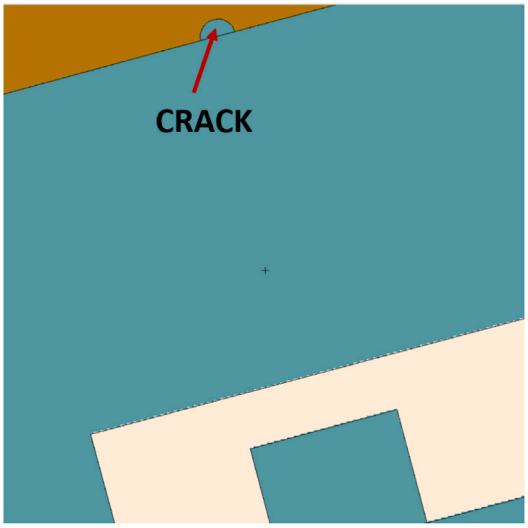

Fig. 14. Vertical 0.1 mm crack in concrete near EVND location in MCNP model.

The error bars in the graph present statistical errors in the calculation, while the error within the nuclear data itself is often left out due to incompleteness in cross section covariance matrices.

In order to get an estimate of the cross section uncertainty, an additional calculation with RR_UNC tool [27] was performed. The RR_UNC program is a specialized tool for calculating uncertainties in neutron-induced reaction rates and cross sections based on ENDF-formatted cross section data and neutron spectra. Its primary function is to facilitate uncertainty propagation, employing standard covariance formulas to account for the variances of cross sections and flux distributions. In particular, it assumes no correlation between the cross section and the neutron flux, simplifying the calculation to the sum of individual relative uncertainties. The code supports providing a reaction rate spectrum as the weighting function; in this case, the flux spectrum is derived by dividing the reaction rate by the corresponding cross sections at infinite dilution. This capability is especially valuable in dosimetry applications or when working with Monte Carlo–generated reaction rate spectra. Additionally, the code has built-in safeguards against anomalous data, such as negative variances or invalid covariance matrices, thereby ensuring robustness and reliability. The well-structured output includes a detailed list of reaction rate uncertainties, as well as tabulated spectra and cumulative integrals.

For this calculation, 640-group neutron spectra were generated using MCNP at three axial sections (bottom, middle and top third of the core) at the gradient chain azimuthal locations. These spectra were then processed in the RR_UNC tool alongside the 640-group IRDFF-II nuclear data library (version 1.05) to determine reaction rates and their associated uncertainties from the covariance matrices. As shown in Fig. 10, the RR_UNC and MCNP reaction rate calculations match closely in the central section of the core. In the lower and upper thirds, however, larger deviations are observed, suggesting that local changes in the neutron spectrum are more pronounced in those regions.

The total uncertainty, derived from cross section covariance matrices, remained nearly constant across all three axial sections. Table 1 reports uncertainty values obtained from the RR_UNC tool. The material number defines mass and atomic number code of parent isotope (cobalt, nickel and iron reactions) and MT reaction type (102 for radiative capture and 103 for proton production).

It can be concluded that the deviation is negligible if different nuclear data libraries are used (see Figs. 25–27), however the uncertainty in nuclear data derived from the cross section variance matrices cannot be neglected and is the highest for the iron reaction (~3%).

Table 1
Neutron spectra statistical uncertainty and cross section uncertainty, calculated with RR_UNC tool.

Mat.	MT	Unc. C.s. [%]	Unc. Sp. [%]	Unc. Total [%]
27 059	102	0.69	0.33	0.76
28 058	103	1.65	0.45	1.71
26 054	103	2.90	0.51	2.94

It can also be concluded that discrepancies between measurements and calculations for cobalt reaction cannot be in full attributed to the nuclear data uncertainty.

4.3.2. Sensitivity to concrete material composition

Due to the proximity of the concrete to the EVND chains, it is assumed that the backscattering of neutrons from the concrete can have a significant influence on the thermal neutron spectrum in the vicinity of the gradient chain. To test this assumption, the neutron flux at the EVND location was compared with the neutron flux before entering the concrete and the subsequent backscattering to the EVND location by the use of flagged tallies. The results are shown in Fig. 11 in three energy groups. The upper limits of the three energy groups were: 0.625 eV (thermal), 0.1 MeV (epithermal) and 20 MeV (fast). The statistical uncertainty of the calculations shown in Fig. 11 is <2%. The neutrons leaving the reactor core are mainly in the fast energy range, some of which are slowed down by water and surrounding structures before they reach the EVND locations. Epithermal and fast neutrons that penetrate the reactor pressure vessel and the air gap are thermalized in the surrounding concrete material, part of which is back-scattered and reaches the EVND locations. And as can be seen in Fig. 11, almost all thermal neutrons that reach the EVND locations originate from the surrounding concrete material. Moreover, the proportion of back-scattered neutrons decreases with increasing neutron energy. This leads to the conclusion that the composition and shape of the concrete material can have a considerable influence on the neutron spectrum (energy distribution of the neutron flux) and the spatial distribution of the neutron flux in the air gap between the reactor pressure vessel and the surrounding concrete. The concrete composition in the current computational model is presented in Table 2.

To assess the extent of sensitivity of the calculated EVND response to the composition of the concrete material (presence of water in the concrete) in two separate analysis. In first analysis, the hydrogen and deuterium isotopes were removed from the concrete while maintaining the original concrete density. In second analysis, the oxygen was reduced by 25% (it was not fully removed because oxygen is present in the concrete also due to presence in aggregate etc.). The results for azimuthal position 0° are shown in Fig. 12, while the results for other azimuthal positions are gathered in Appendix B.

It can be observed that, as expected, the measured iron and nickel reactions in the gradient chains are less sensitive to changes in concrete composition, but for the cobalt reaction rates in the gradient chains the deviations are up to ~30% for removal of hydrogen and ~5% for 25% reduction in oxygen. This is due to the different energy dependence of the reaction cross-section (see Appendix C). The reactions measured on iron and nickel are threshold reactions, while the reaction measured on cobalt is also sensitive to thermal neutrons. Hydrogen and oxygen in concrete acts as a neutron moderator and reflector, back-scattering thermal neutrons from the concrete to the gradient chains. Removing the hydrogen from the concrete, as expected, resulted in significant decrease in the cobalt reaction rate, while the effect of oxygen is significantly lower.

4.3.3. Sensitivity to concrete geometry

The sensitivity of the EVND gradient chains to a possible deviation of the surrounding concrete radius was investigated. For this purpose, the radius of the concrete was changed from the reference value of

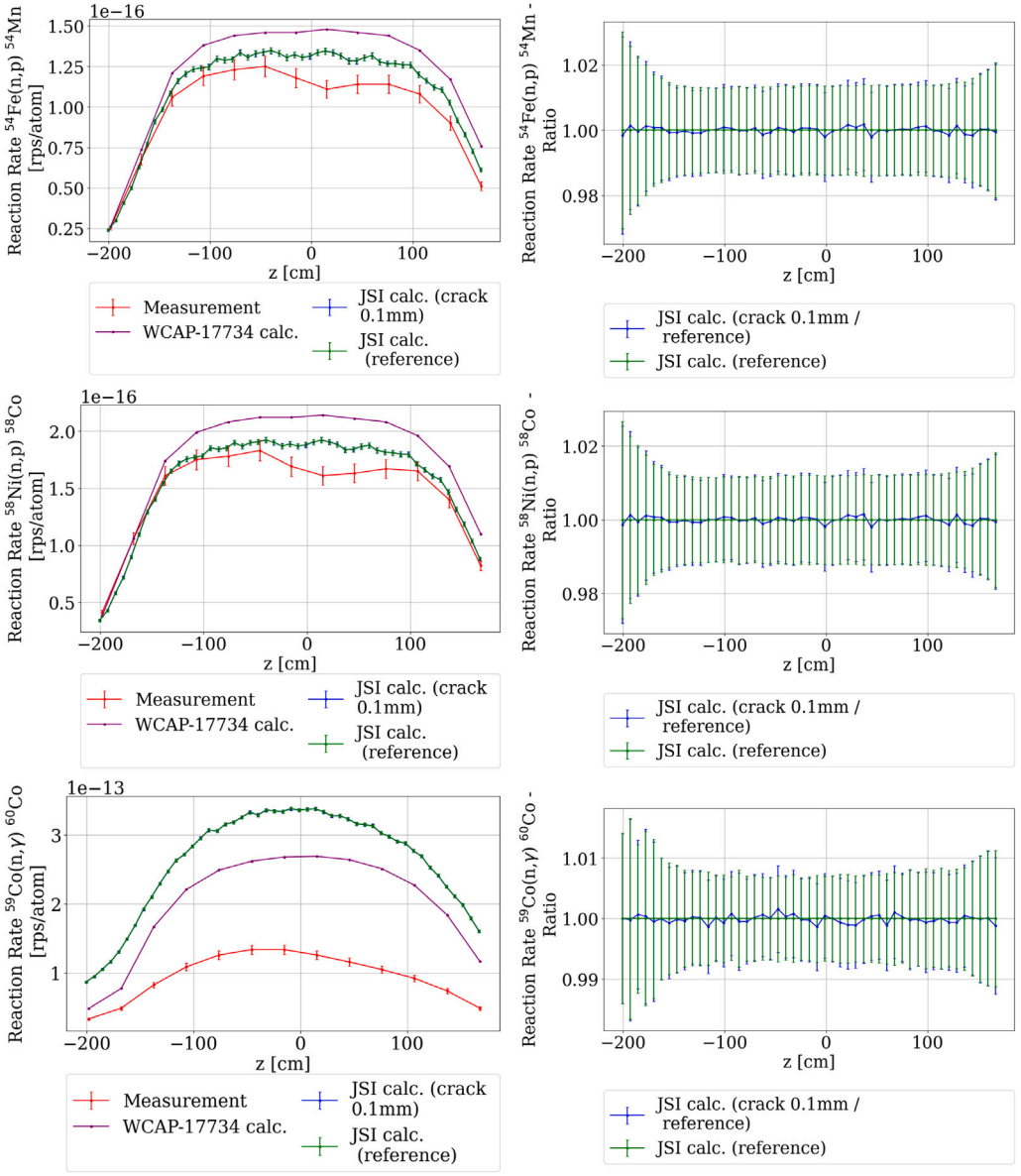

Fig. 15. Measured ^{54}Fe(n,p) (top), ^{58}Ni(n,p) (middle) and ^{59}Co(n,γ) (bottom) reaction rates in gradient chains sensitivity to 0.1 mm cracks in the surrounding concrete at location 0° (top), 15° (middle) and 30° (bottom). Calculations with 0.1 mm cracks in the concrete surrounding the reactor pressure vessel are marked in blue, reference calculations with reference concrete composition are marked in green. The diagrams on the left show the axial profiles of the gradient chain and the diagrams on the right show the relative deviations between the different concrete geometries. The connecting lines serve as an eye guide only. (For interpretation of the references to color in this figure legend, the reader is referred to the web version of this article.)

200.6 cm by +5 cm (to 205.6 cm). The radial reference position of gradient chains was 197.65 cm, which means that they were close to the reference concrete radius. To investigate the case of a radius smaller than the reference radius, the radius was changed to 199 cm, which seems reasonable due to the proximity of the dosimeters. The results for azimuthal position 0° are shown in Fig. 13, while the supplementary results for positions at 15° and 30° are shown in Appendix B. The results show that the cobalt reaction rate in the gradient chain is most sensitive to deviations of the concrete radius, with the deviations being ~5%. In the case of the measured ^{58}Ni(n,p) and ^{54}Fe(n,p) reaction rates in gradient chains, the deviations are negligible. As with the sensitivity to the concrete composition, the energy dependence of the reaction cross-section is the reason for the higher sensitivity of the measured ^{59}Co(n,γ) reaction rates in gradient chains, since the reaction is also sensitive to thermal neutrons back-scattered from the concrete.

The sensitivity to possible cracks in the concrete structure was also investigated. It was estimated that the expected width of the cracks in the concrete at NEK is <0.1 mm. For the calculation, vertical cracks in the concrete surface were added in the geometry model of the surrounding concrete at the same azimuthal positions where the gradient chains were located (see Fig. 14). Cracks with a diameter of 0.1 mm were considered. The results for azimuthal location at 0° are summarized in Fig. 15, while supplementary results for other azimuthal locations are gathered in Appendix B. It can be concluded that the 0.1 mm crack near the dosimeter sets does not affect the measurements.

4.3.4. *Sensitivity to position*

The effect of uncertainty in the positions of the gradient chain and dosimeter sets on the calculated EVND results was investigated by shifting the EVND gradient chains in the radial and azimuthal directions to examine the difference in their response. Fig. 16 shows the results for the radial shift of the gradient chains for azimuthal position at 0°. Results for other azimuthal positions are presented in Appendix B. It can be observed that the response of the reaction rates of iron

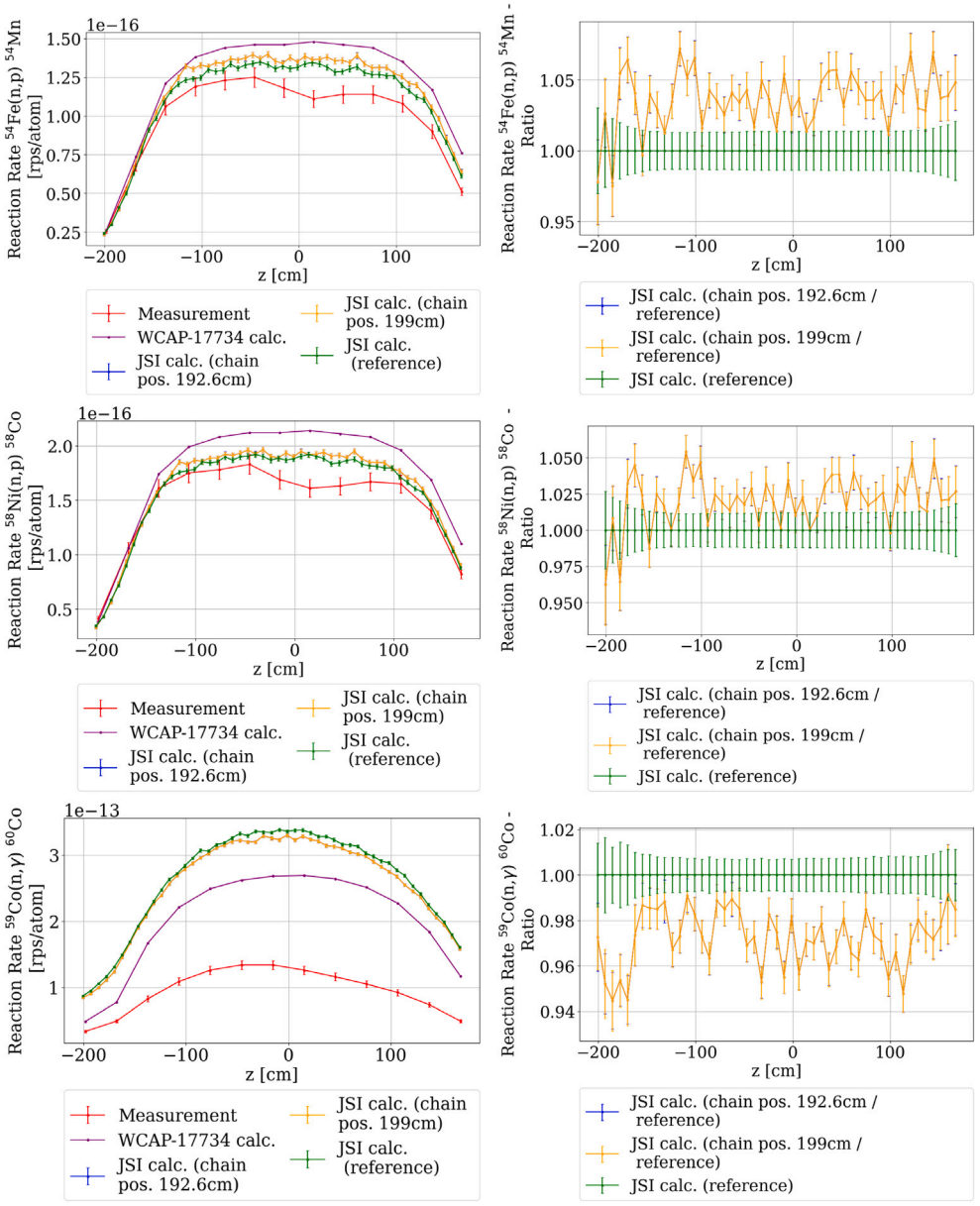

Fig. 16. Measured ^{54}Fe(n,p) (top), ^{58}Ni(n,p) (middle) and ^{59}Co(n,γ) (bottom) reaction rates in gradient chains sensitivity to radial position at location 0°. Calculations in which the gradient chains were radially shifted 5.05 cm closer to the reactor core are marked in blue, calculations in which the gradient chains were radially shifted 1.35 cm further from the reactor core are marked in blue, reference calculations with reference concrete composition are marked in green. The diagrams on the left show the axial profiles of the gradient chains and the diagrams on the right show the relative deviation between different radial positions. The connecting lines serve as an eye guide only. (For interpretation of the references to color in this figure legend, the reader is referred to the web version of this article.)

and nickel in the gradient chains is less sensitive to position changes, with the observed deviations being within the statistical uncertainties. However, in the case of the measured ^{59}Co(n,γ) reaction rate in the gradient chains, the deviations become significant and can contribute up to ~5% for a radial displacement of 5 cm, which corresponds to a radial gradient of about 1%/cm. This can again be explained by the sensitivity of the measured ^{59}Co(n,γ) reaction rate in gradient chains to thermal neutrons, which, as shown in previous sensitivity studies, are significantly influenced by the surrounding concrete.

Fig. 17 shows the sensitivities to azimuthal shifts of the gradient chains at azimuthal location 0°. Results for other azimuthal positions (15° and 30°) are presented in Appendix B. For all three gradient chains, similar results can be observed, with the largest average deviation between all gradient chains observed at the 15° position. Different sensitivities depending on the azimuthal positions can be explained by the different concrete and core shape near individual azimuthal positions (see Fig. 5). The core shape affects the neutron flux azimuthal distribution exiting the reactor pressure vessel (see Fig. 18).

At 0° there is no concrete near the gradient chain and a displacement of ±5° is symmetric with respect to the surrounding concrete shape. Moving the gradient chain closer to the concrete results in the sensors being irradiated in a higher thermal neutron flux due to back-scattering by the concrete. This is supported by the observation of the sensitivity of the different gradient chains in the 0° position compared to the azimuthal shift. It can be observed that the sensitivities of the measured iron and nickel reaction rates in gradient chains can be considered negligible since threshold reactions are measured, and that for the measured ^{59}Co(n,γ) reaction rates in the gradient chains, the sensitivity to the azimuthal shift of +5° and −5° is comparable, ~3%. For gradient chains in the 15° position (see Appendix B), similar

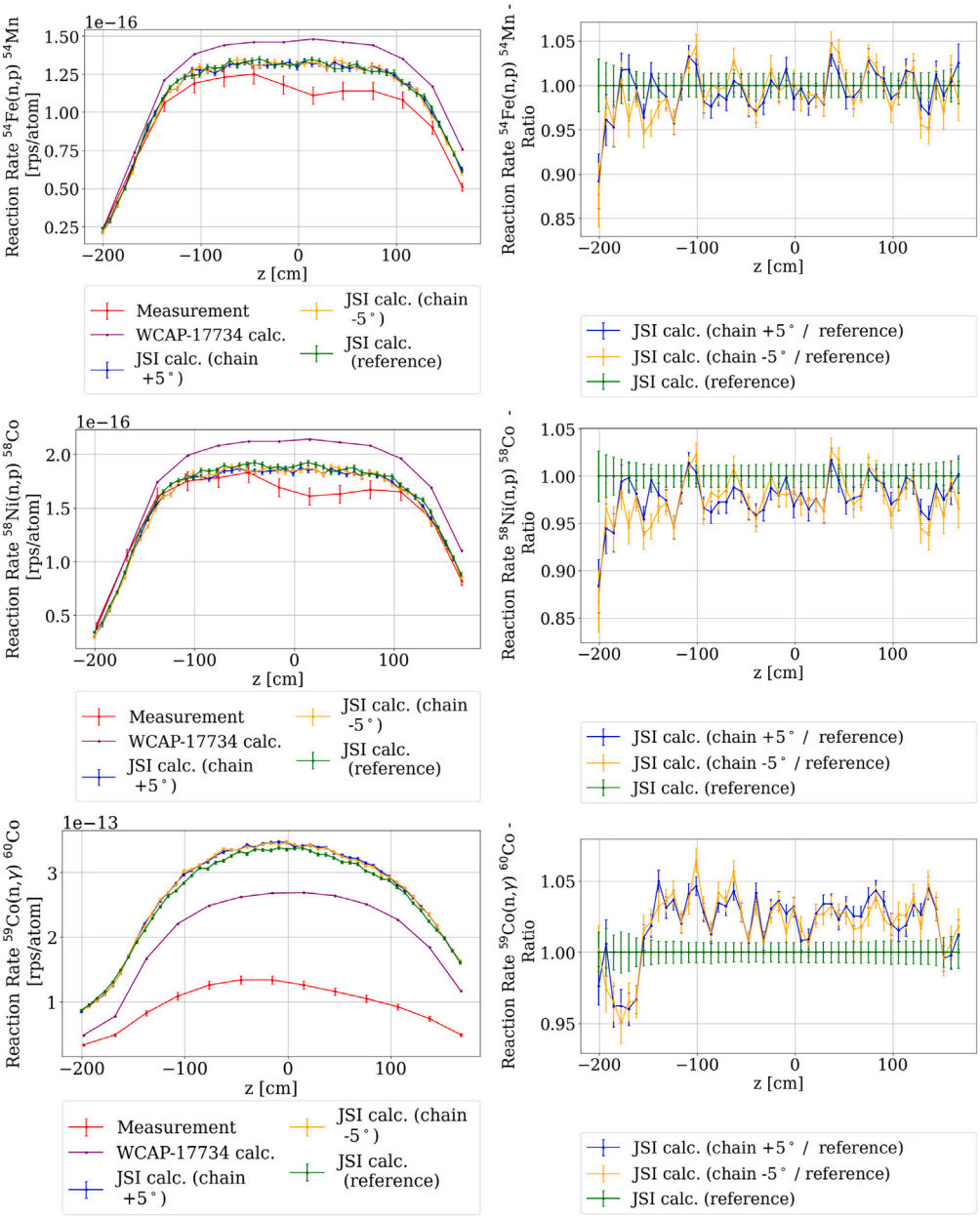

Fig. 17. Measured ^{54}Fe(n,p) (top), ^{58}Ni(n,p) (middle) and ^{59}Co(n,γ) (bottom) reaction rates in gradient chains sensitivity to azimuthal position at location 0°. Calculations with an azimuthal shift of +5° are marked in blue, calculations with an azimuthal shift of −5° are marked in orange, reference calculations with the reference chain position are marked in green. The diagrams on the left show the axial profiles of the gradient chain and the diagrams on the right show the relative deviations between the different azimuthal positions. The connecting lines serve as an eye guide only. (For interpretation of the references to color in this figure legend, the reader is referred to the web version of this article.)

sensitivities are observed between different reactions, leading to the conclusion that the reason for the deviation is not only due to the shape of the concrete (which is approximately the same for an azimuthal shift of ±5°). To explain the observed deviations, we need to consider the shape of the core and the azimuthal deviations in the neutron flux exiting the reactor pressure vessel (see Fig. 18). Near the 15° position there is a fuel element at the edge (fuel element F13, see Fig. 3) and at a +5° displacement causes the gradient chain to move further away from this FA, towards the empty fuel position. This is the reason for the decrease in the neutron flux at this position (see Fig. 18) and the decrease in the gradient chain response, which is proportional to the decrease in neutron flux and is ~10% for the reaction rates of iron and nickel in the gradient chains and ~7% for the reaction rate of cobalt in gradient chains. Neutrons escaping from the reactor core are mainly fast and therefore the highest sensitivity is observed for the iron and nickel reaction rates in the gradient chains, while the cobalt reaction in the gradient chains is less sensitive to changes in fast neutron flux due to its sensitivity to thermal neutrons. When the gradient chain in the 15° position is shifted by −5°, it is closer to two FAs (F-13 and G-13, see Fig. 3) and the fast neutron flux at this position increases (see Fig. 18). For the gradient chain in the 30° position, a similar effect as for the 15° position can be observed (see Appendix B).

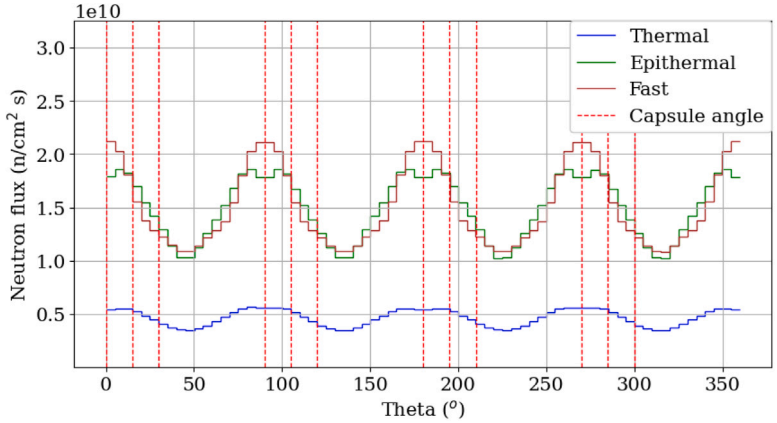

Fig. 18. Neutron flux at the exit of reactor pressure vessel with indicated capsule angles. Neutron flux is averaged over entire core height.

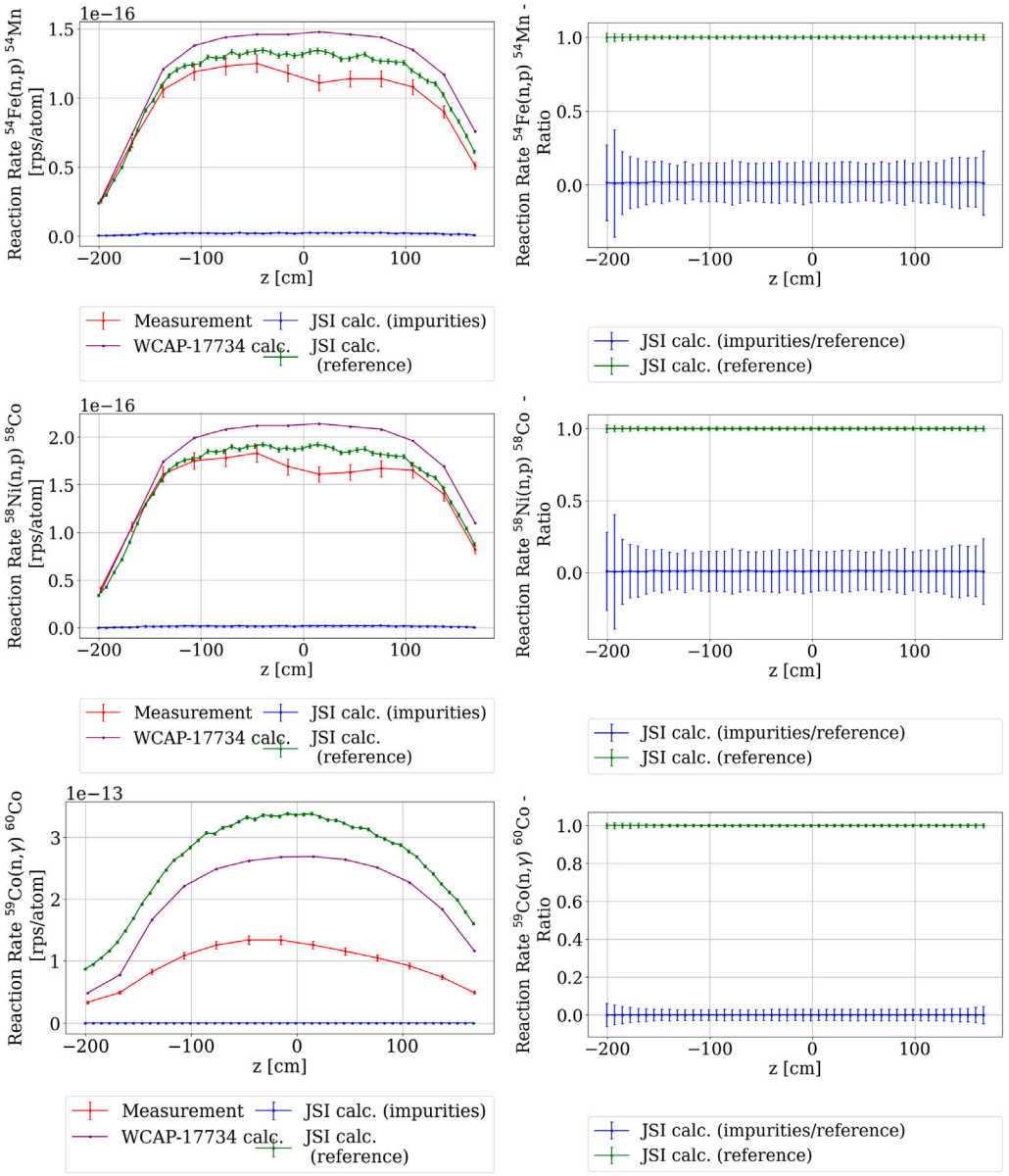

Fig. 19. Measured ^{54}Fe(n,p) (top), ^{58}Ni(n,p) (middle) and ^{59}Co(n,γ) (bottom) reaction rates in gradient chains sensitivity to the presence of impurities in sample at location 0°. Calculations for impurities are marked in blue, reference calculations without impurities are marked in green. The diagrams on the left show the axial profiles of the gradient chains and the diagrams on the right show the relative differences in reaction rates. The connecting lines serve as an eye guide only. (For interpretation of the references to color in this figure legend, the reader is referred to the web version of this article.)

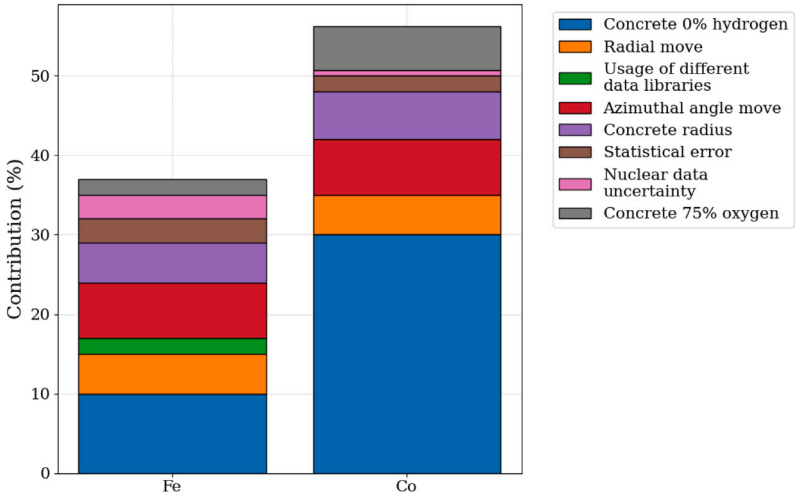

Fig. 20. Cumulative graph of various sensitivity effects for Fe and Co reactions.

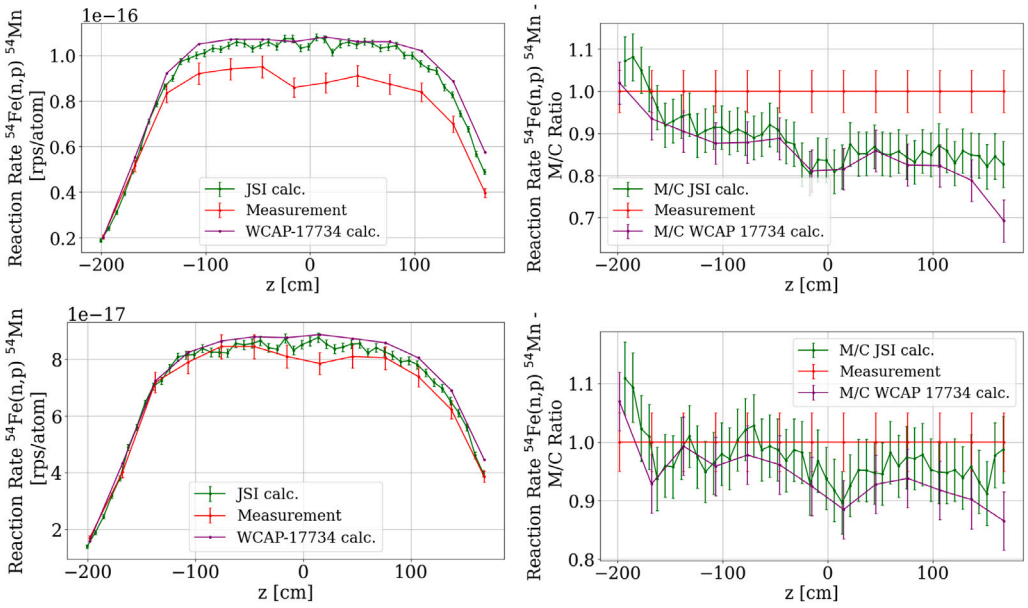

Fig. 21. Gradient chain at location 15° (top) and 30° (bottom), ^{54}Fe(n,p)^{54}Mn reaction rate. The red color stands for measurements, the purple color for Westinghouse calculations [3] and the green color for MCNP calculations. The diagrams on the left show the axial profiles of the gradient chain and the diagrams on the right show the relative deviation of the different calculations from the measurement. The connecting lines serve as an eye guide only. The error bars represent 1 σ uncertainties. (For interpretation of the references to color in this figure legend, the reader is referred to the web version of this article.)

4.3.5. Sensitivity to impurities in samples

The material analysis of the dosimetry foils can be found in the Ref. [28], where impurities and masses for individual foils are listed. To test the sensitivity of the EVND calculations with respect to the impurities present in the activation foils, the possible reactions of the impurities contributing to the same product measured in the primary reaction in gradient chains were determined as follows: ^{55}Mn(n,2n)^{54}Mn for measured ^{54}Fe(n,p) reaction rates, ^{59}Co(n,2n)^{58}Co for measured ^{58}Ni(n,p) reaction rates, ^{60}Ni(n,p)^{60}Co for measured ^{59}Co(n,γ) reaction rates. The reaction rates for the reactions from the impurities present in the sample were calculated at the EVND gradient chain locations and compared to the primary reactions measured in gradient chains. Results are shown in Fig. 19 for azimuthal position at 0°, while the results for other azimuthal positions are gathered in Appendix B. It can be observed that all additional reactions have a negligible effect compared to the primary reaction. It can therefore be concluded that impurities have a negligible influence on the measurements.

The effect of the presence of impurities in the measured sample was also tested using the FISPACT-II inventory and source term code [29], where the isotopic composition of the sample was simulated both with and without impurities over the entire fuel cycle and the deviations in the inventory of measured isotopes were analyzed. FISPACT-II is a versatile code for the calculation of nuclear transmutation, activation and decay. The code is ideal for evaluating and predicting changing radionuclide concentrations during irradiation. FISPACT-II utilizes extensive nuclear data libraries and contains cross-sectional data for various nuclear reactions. The built-in algorithms allow the use of any energy group structure. For the FISPACT-II calculations, the 709 group neutron spectra and flux levels at the EVND foil locations, calculated with MCNP were used as input variables. As the IRDFF-II library has an incomplete isotope list, it is not suitable for depletion modeling; therefore, the ENDF-VIII.0 library was used instead. The results showed a negligible influence (within the uncertainties) of the impurities on the measured isotope activities for all foils.

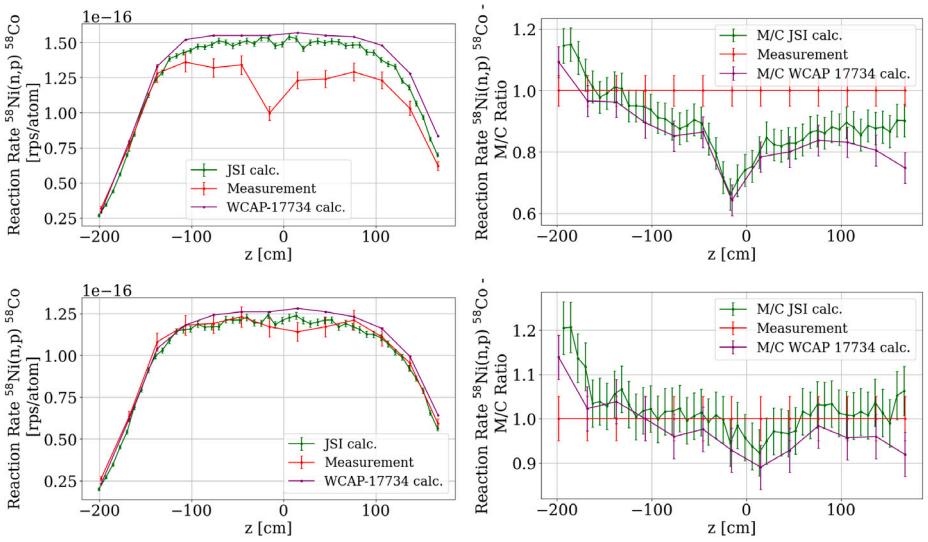

Fig. 22. Gradient chain at location 15° (top) and 30° (bottom), ^{58}Ni(n,p)^{58}Co reaction rate. The red color stands for measurements, the purple color for Westinghouse calculations [3] and the green color for MCNP calculations. The diagrams on the left show the axial profiles of the gradient chain and the diagrams on the right show the relative deviation of the different calculations from the measurement. The connecting lines serve as an eye guide only. The error bars represent 1 σ uncertainties.

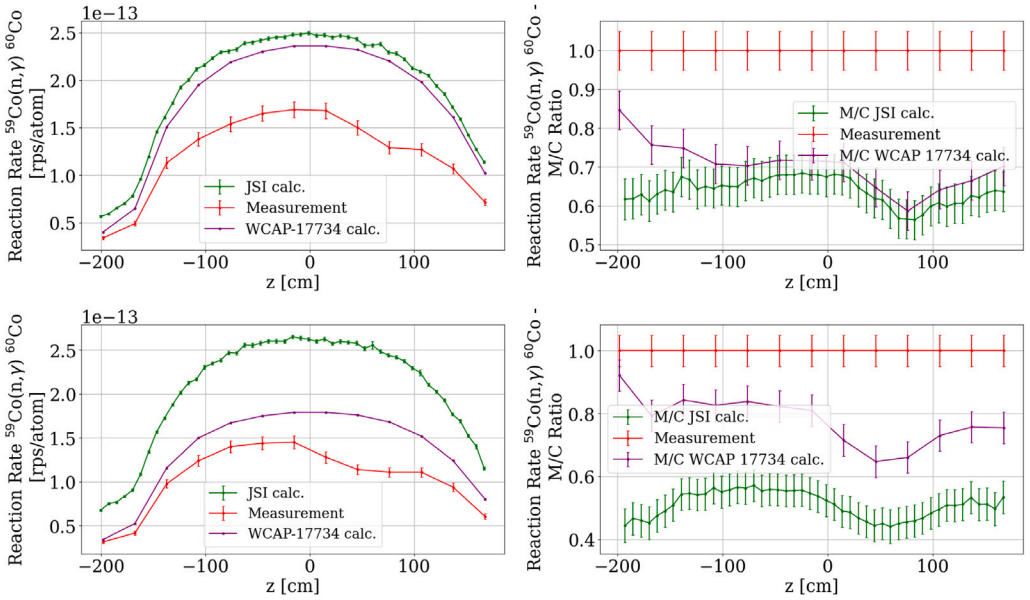

Fig. 23. Gradient chain at location 15° (top) and 30° (bottom), ^{59}Co(n,γ)^{60}Co reaction rate. The red color stands for measurements, the purple color for Westinghouse calculations [3] and the green color for MCNP calculations. The diagrams on the left show the axial profiles of the gradient chain and the diagrams on the right show the relative deviation of the different calculations from the measurement. The connecting lines serve as an eye guide only. The error bars represent 1 σ uncertainties. (For interpretation of the references to color in this figure legend, the reader is referred to the web version of this article.)

4.3.6. Cumulative effect of different sensitivities

In Fig. 20, we observe the cumulative graph of various sensitivity effects for Fe and Co reactions, representing examples sensitive to fast and thermal neutrons, respectively. The analysis of multiple sensitivity effects indicates that reaction rates can generally be assessed on an order of magnitude scale. The primary effect to the computational bias, due to not accurately knowing the experimental conditions, is due to the hydrogen content in concrete, which warrants further investigation. It is important to note that hydrogen's influence is much more pronounced in reactions involving thermal neutrons. Therefore, additional research is suggested, particularly for refining radioactive inventory predictions, as opposed to radiation damage assessments, which are predominantly driven by fast neutrons.

Although several sensitivity effects have been discussed in this paper, numerous other possible sensitivity scenarios remain. For instance, the primary water temperature profile was simplified outside the core barrel region by assuming a uniform temperature. Due to the lack of detailed data and the complexity of multiphysics simulations, the impact of water temperature is still not thoroughly investigated. According to [30], a 1 K change in water temperature can affect the results by approximately 1%. Another factor involves deviations in the power profile, which may occur due to unexpected changes in fuel elements. However, strict monitoring of the power profile in fuel assemblies and quadrant tilts is conducted, as referenced in [31]. Given that neutron flux magnitude is closely correlated with power levels, even a maximum power tilt of a few percent would only affect the reaction rates by a similar few percent.

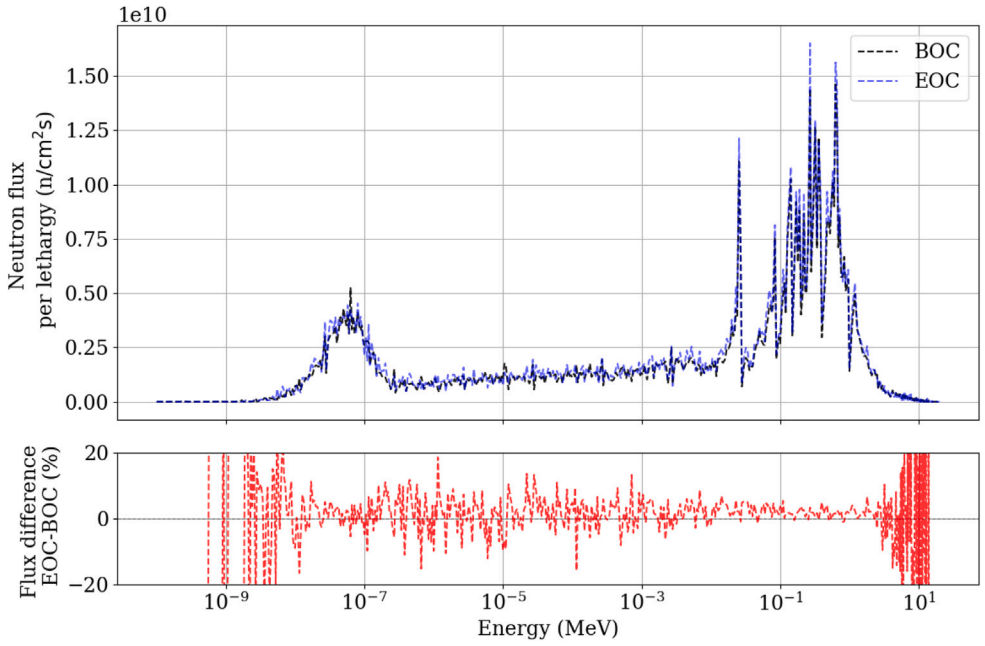

Fig. 24. Comparison between BOC and EOC normalized neutron flux per unit lethargy at the site of the 0° middle EVND capsule.

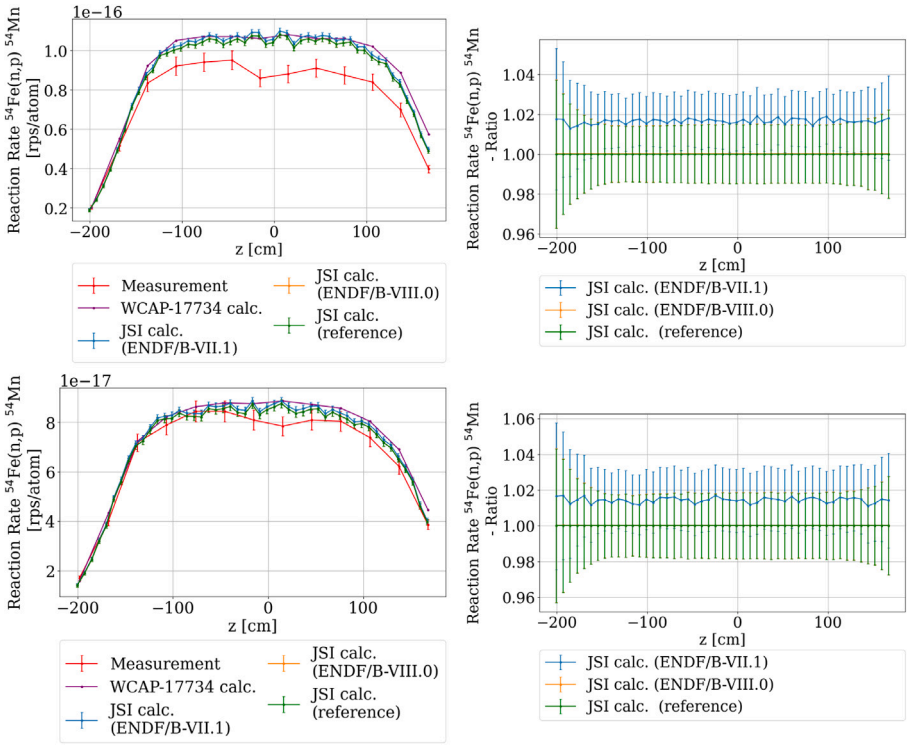

Fig. 25. Measured ^{54}Fe(n,p) reaction rate in gradient chains sensitivity to nuclear data libraries at location 15° (top) and 30° (bottom). Calculations with ENDF/B-VII.1 are shown in blue, calculations with ENDF/B-VIII.0 in orange and reference calculations with the IRDFF-II nuclear data library in green. The diagrams on the left show the axial profiles of the gradient chain and the diagrams on the right show the relative deviations of the different nuclear data libraries from the "reference source". The connecting lines serve as an eye guide only. (For interpretation of the references to color in this figure legend, the reader is referred to the web version of this article.)

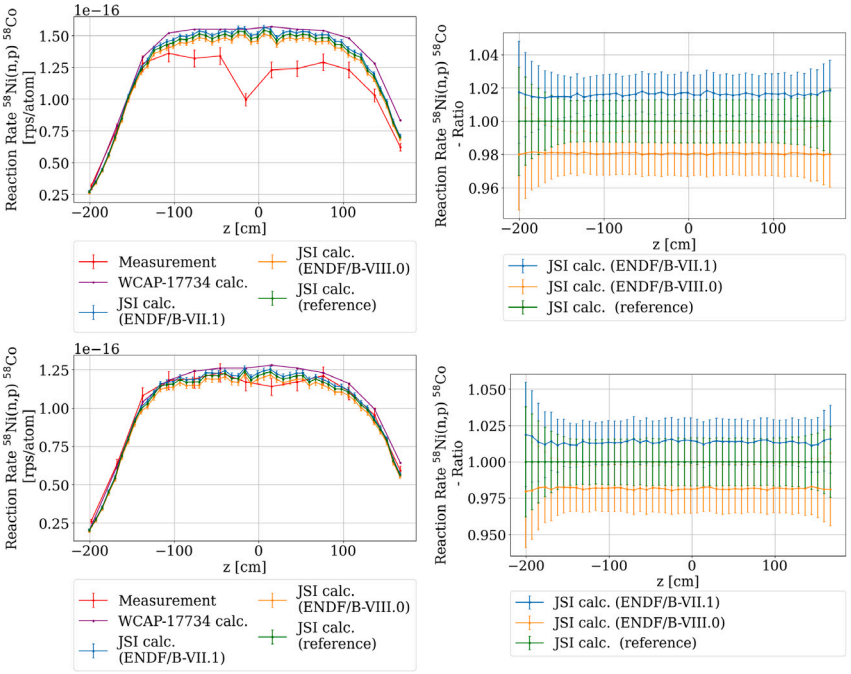

Fig. 26. Measured ^{58}Ni(n,p) reaction rates in gradient chains sensitivity to nuclear data libraries at location 15° (top) and 30° (bottom). Calculations with ENDF/B-VII.1 are shown in blue, calculations with ENDF/B-VIII.0 in orange and reference calculations with the IRDFF-II nuclear data library in green. The diagrams on the left show the axial profiles of the gradient chain and the diagrams on the right show the relative deviations of the different nuclear data libraries from the "reference source". The connecting lines serve as an eye guide only. (For interpretation of the references to color in this figure legend, the reader is referred to the web version of this article.)

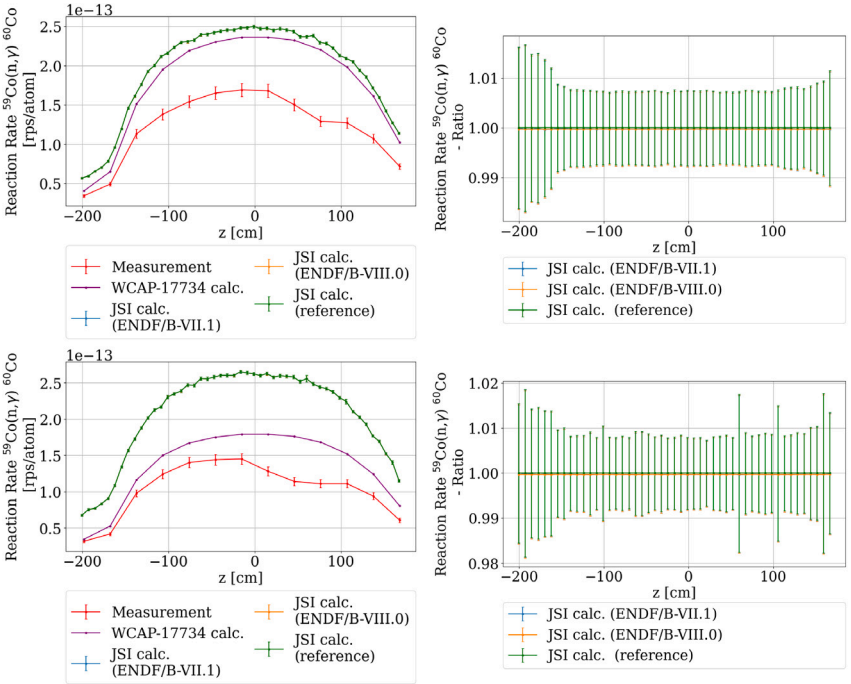

Fig. 27. Measured ^{59}Co(n,γ) reaction rates in gradient chains sensitivity to nuclear data libraries at location 15° (top) and 30° (bottom). Calculations with ENDF/B-VII.1 are shown in blue, calculations with ENDF/B-VIII.0 in orange and reference calculations with the IRDFF-II nuclear data library in green. The diagrams on the left show the axial profiles of the gradient chain and the diagrams on the right show the relative deviations of the different nuclear data libraries from the "reference source". The connecting lines serve as an eye guide only. (For interpretation of the references to color in this figure legend, the reader is referred to the web version of this article.)

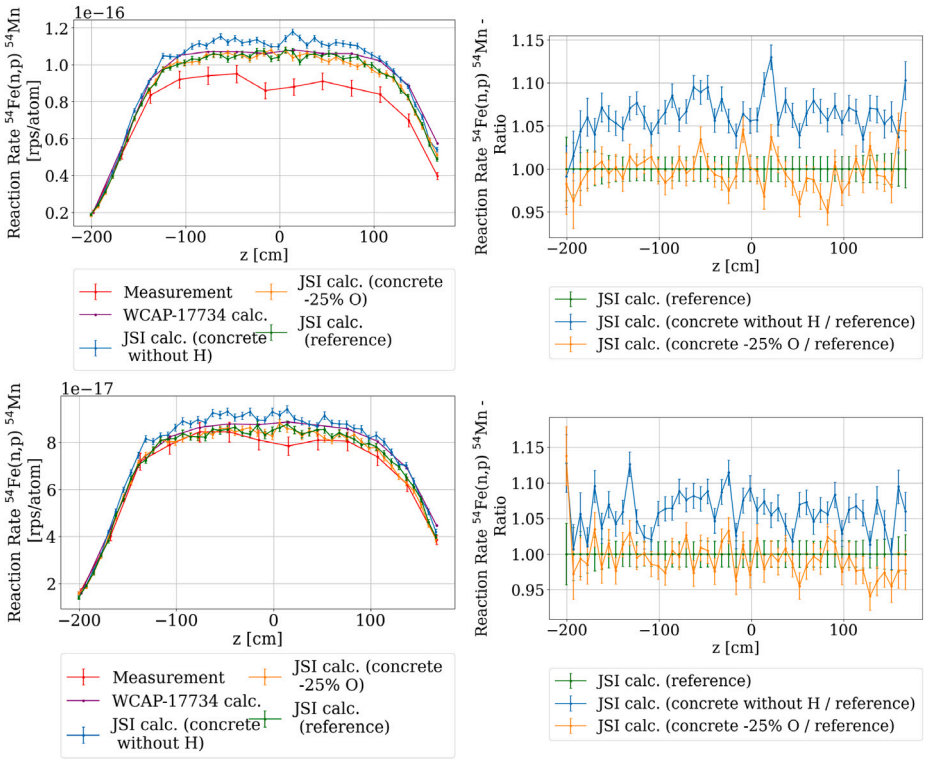

Fig. 28. Measured ^{54}Fe(n,p) reaction rates in gradient chains sensitivity to water content in surrounding concrete at location 15° (top) and 30° (bottom). Calculations without hydrogen in the concrete surrounding reactor pressure vessel are marked in blue, with reduced oxygen for ~25% in yellow, reference calculations with reference concrete composition are marked in green. The diagrams on the left show the axial profiles of the gradient chains and the diagrams on the right show the relative deviation between the different concrete compositions. The connecting lines serve as an eye guide only. (For interpretation of the references to color in this figure legend, the reader is referred to the web version of this article.)

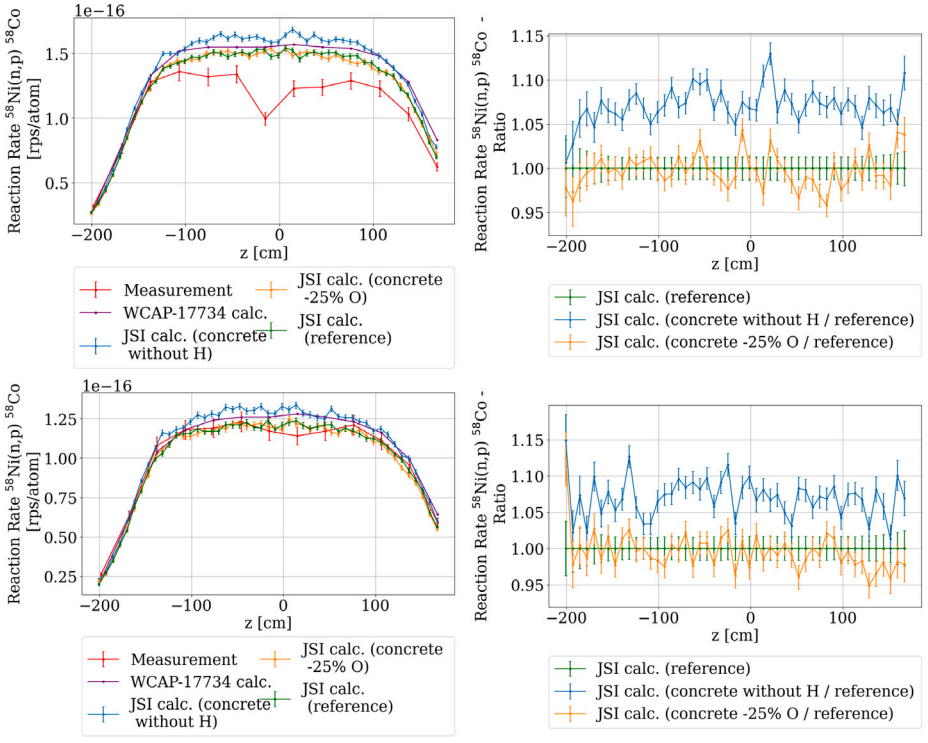

Fig. 29. Measured ^{58}Ni(n,p) reaction rates in gradient chains sensitivity to water content in surrounding concrete at location 15° (top) and 30° (bottom). Calculations without hydrogen in the concrete surrounding reactor pressure vessel are marked in blue, with reduced oxygen for ~25% in yellow, reference calculations with reference concrete composition are marked in green. The diagrams on the left show the axial profiles of the gradient chains and the diagrams on the right show the relative deviation between the different concrete compositions. The connecting lines serve as an eye guide only. (For interpretation of the references to color in this figure legend, the reader is referred to the web version of this article.)

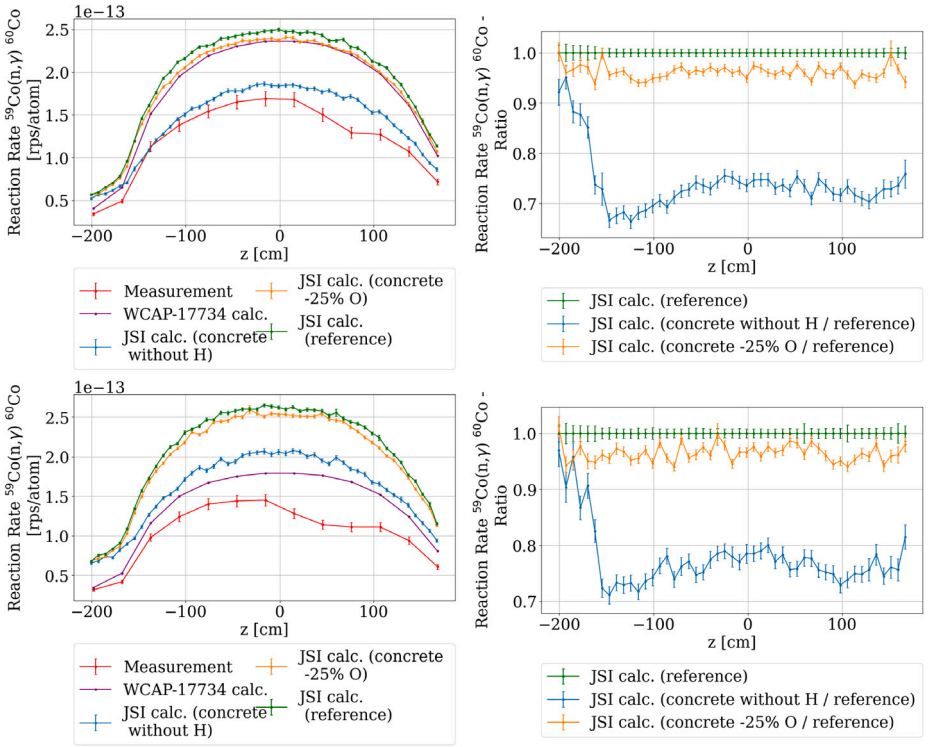

Fig. 30. Measured ^{59}Co(n,γ) reaction rates in gradient chains sensitivity to water content in surrounding concrete at location 15° (top) and 30° (bottom). Calculations without hydrogen in the concrete surrounding reactor pressure vessel are marked in blue, with reduced oxygen for ~25% in yellow, reference calculations with reference concrete composition are marked in green. The diagrams on the left show the axial profiles of the gradient chains and the diagrams on the right show the relative deviation between the different concrete compositions. The connecting lines serve as an eye guide only. (For interpretation of the references to color in this figure legend, the reader is referred to the web version of this article.)

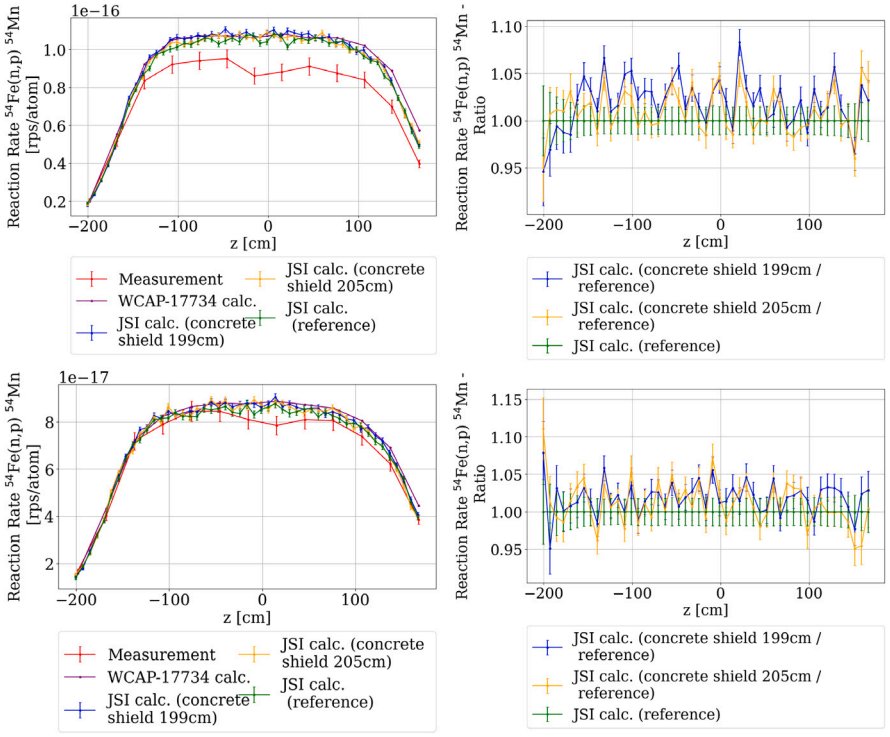

Fig. 31. Measured ^{54}Fe(n,p) reaction rates in gradient chains sensitivity to surrounding concrete radius at location 15° (top) and 30° (bottom). Calculations with a smaller concrete radius (199 cm) are marked in blue, calculations with a larger concrete radius (205.6 cm) are marked in orange, reference calculations with a reference concrete radius (200.6 cm) are marked in green. The diagrams on the left show the axial profiles of the gradient chain and the diagrams on the right show the relative deviations between the different concrete geometries. The connecting lines serve as an eye guide only. (For interpretation of the references to color in this figure legend, the reader is referred to the web version of this article.)

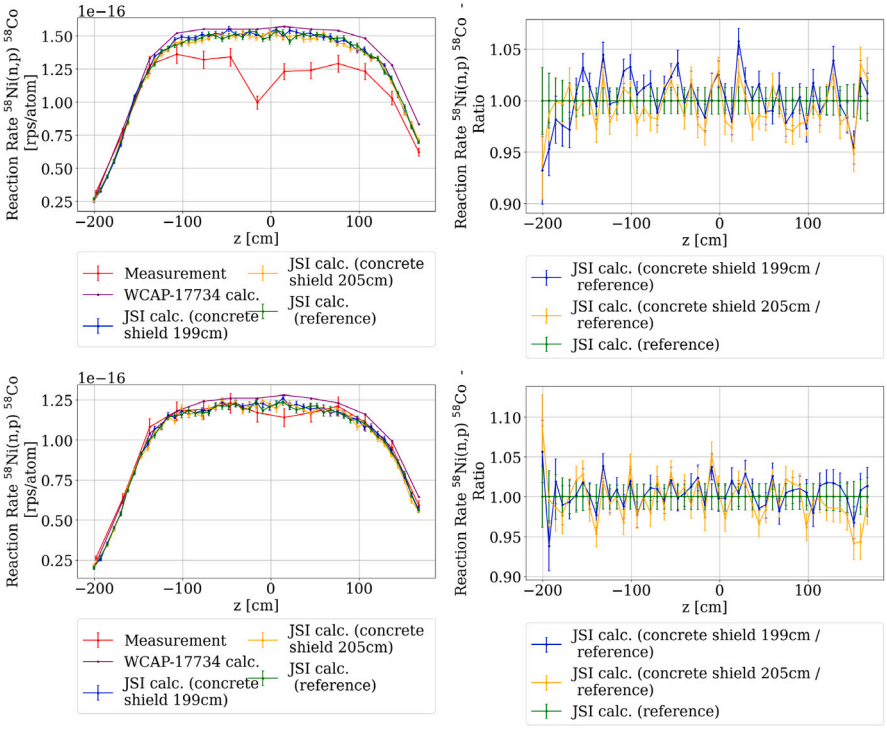

Fig. 32. Measured ^{58}Ni(n,p) reaction rates in gradient chains sensitivity to surrounding concrete radius at location 15° (top) and 30° (bottom). Calculations with a smaller concrete radius (199 cm) are marked in blue, calculations with a larger concrete radius (205.6 cm) are marked in orange, reference calculations with a reference concrete radius (200.6 cm) are marked in green. The diagrams on the left show the axial profiles of the gradient chain and the diagrams on the right show the relative deviations between the different concrete geometries. The connecting lines serve as an eye guide only. (For interpretation of the references to color in this figure legend, the reader is referred to the web version of this article.)

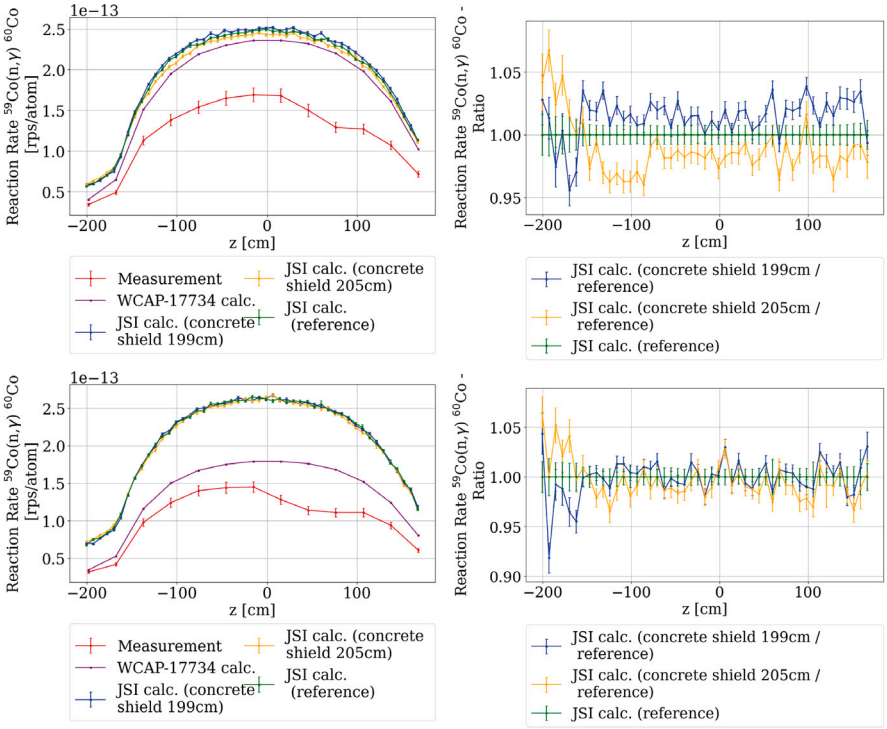

Fig. 33. Measured ^{59}Co(n,γ) reaction rates in gradient chains sensitivity to surrounding concrete radius at location 15° (top) and 30° (bottom). Calculations with a smaller concrete radius (199 cm) are marked in blue, calculations with a larger concrete radius (205.6 cm) are marked in orange, reference calculations with a reference concrete radius (200.6 cm) are marked in green. The diagrams on the left show the axial profiles of the gradient chain and the diagrams on the right show the relative deviations between the different concrete geometries. The connecting lines serve as an eye guide only. (For interpretation of the references to color in this figure legend, the reader is referred to the web version of this article.)

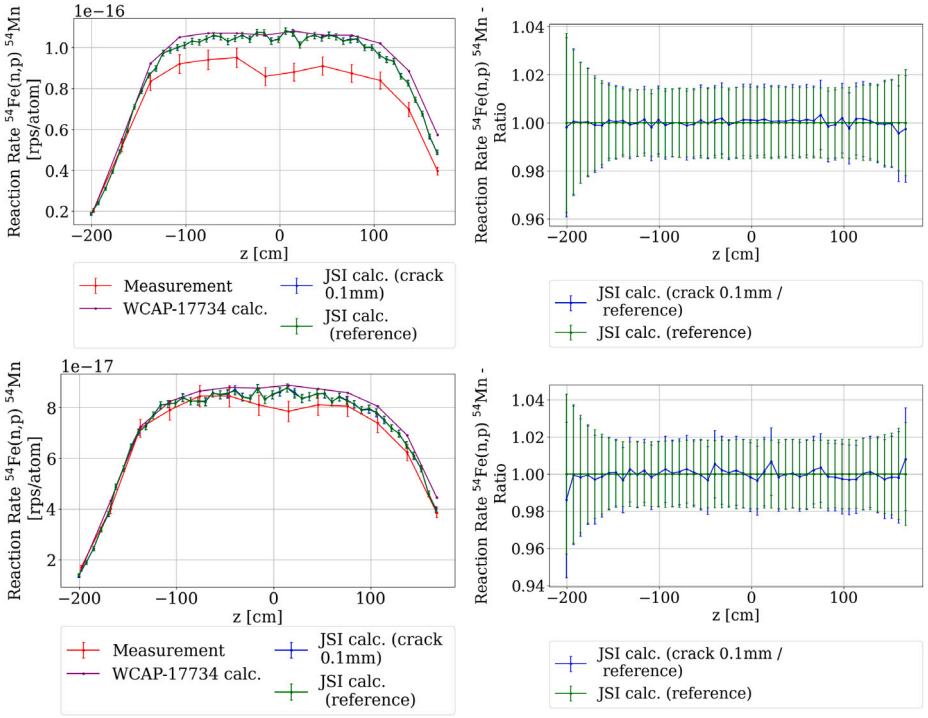

Fig. 34. Measured ^{54}Fe(n,p) reaction rates in gradient chains sensitivity to 0.1 mm cracks in the surrounding concrete at location 15° (top) and 30° (bottom). Calculations with 0.1 mm cracks in the concrete surrounding the reactor pressure vessel are marked in blue, reference calculations with reference concrete composition are marked in green. The diagrams on the left show the axial profiles of the gradient chain and the diagrams on the right show the relative deviations between the different concrete geometries. The connecting lines serve as an eye guide only. (For interpretation of the references to color in this figure legend, the reader is referred to the web version of this article.)

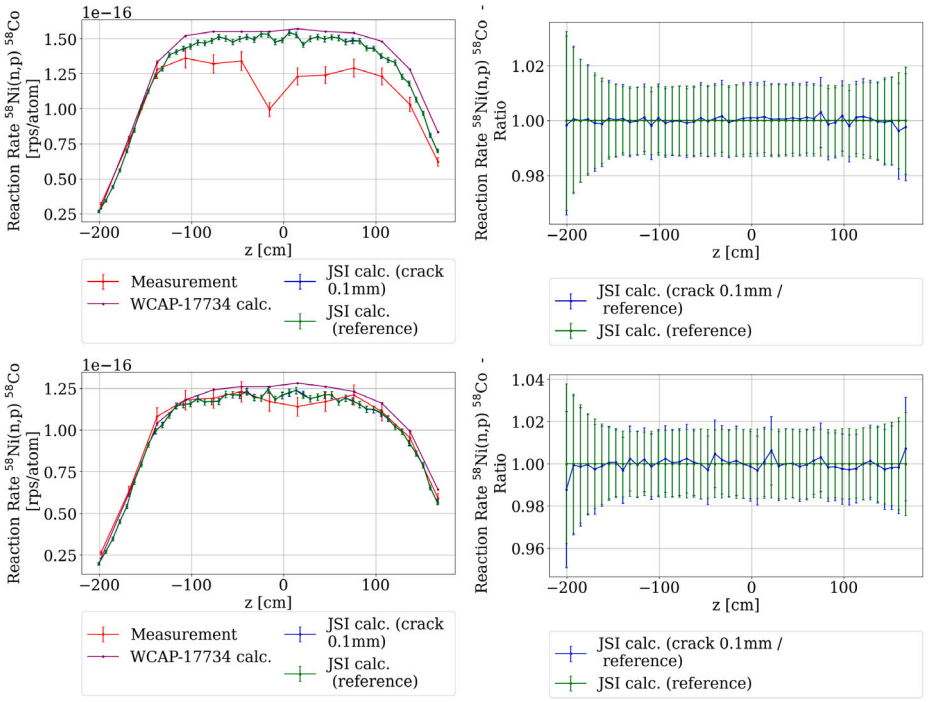

Fig. 35. Measured ^{58}Ni(n,p) reaction rates in gradient chains sensitivity to 0.1 mm crack in surrounding concrete at location 15° (top) and 30° (bottom). Calculations with 0.1 mm cracks in the surrounding concrete. Calculations with 0.1 mm cracks in the concrete surrounding the reactor pressure vessel are marked in blue, reference calculations with reference concrete composition are marked in green. The diagrams on the left show the axial profiles of the gradient chain and the diagrams on the right show the relative deviations between the different concrete geometries. The connecting lines serve as an eye guide only. (For interpretation of the references to color in this figure legend, the reader is referred to the web version of this article.)

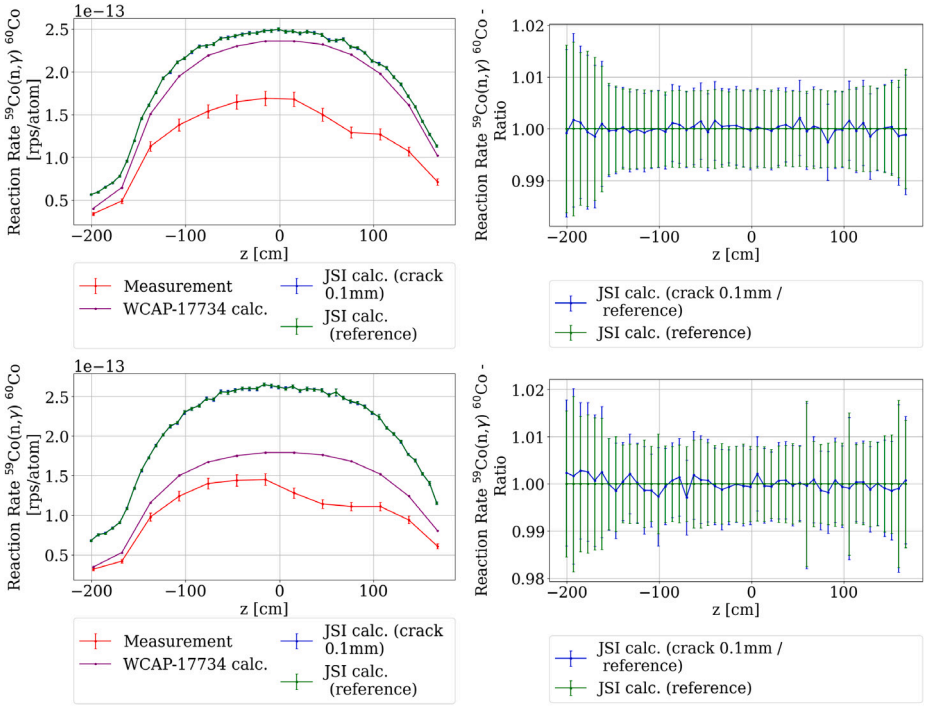

Fig. 36. Measured ^{59}Co(n,γ) reaction rates in gradient chains sensitivity to 0.1 mm crack in surrounding concrete at location 15° (top) and 30° (bottom). Calculations with 0.1 mm cracks in the surrounding concrete. Calculations with 0.1 mm cracks in the concrete surrounding the reactor pressure vessel are marked in blue, reference calculations with reference concrete composition are marked in green. The diagrams on the left show the axial profiles of the gradient chain and the diagrams on the right show the relative deviations between the different concrete geometries. The connecting lines serve as an eye guide only. (For interpretation of the references to color in this figure legend, the reader is referred to the web version of this article.)

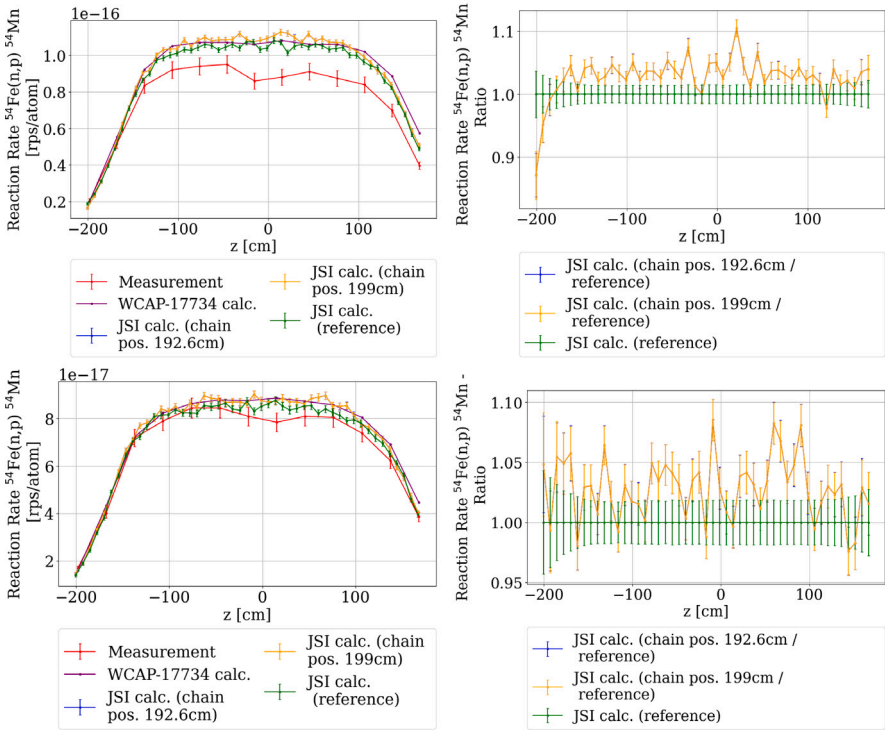

Fig. 37. Measured ^{54}Fe(n,p) reaction rates in gradient chains sensitivity to radial position at location 15° (top) and 30° (bottom). Calculations in which the gradient chains were radially shifted 5.05 cm closer to the reactor core are marked in blue, calculations in which the gradient chains were radially shifted 1.35 cm further from the reactor core are marked in blue, reference calculations with reference concrete composition are marked in green. The diagrams on the left show the axial profiles of the gradient chains and the diagrams on the right show the relative deviation between different radial positions. The connecting lines serve as an eye guide only. (For interpretation of the references to color in this figure legend, the reader is referred to the web version of this article.)

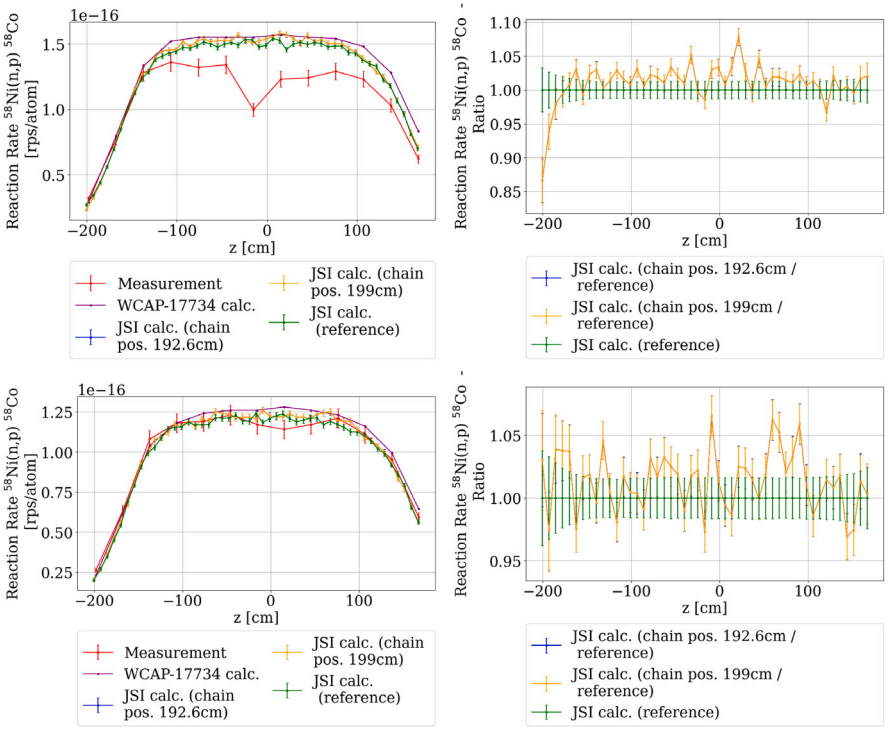

Fig. 38. Measured ^{58}Ni(n,p) reaction rates in gradient chains sensitivity to radial position at location 15° (top) and 30° (bottom). Calculations in which the gradient chains were radially shifted 5.05 cm closer to the reactor core are marked in blue, calculations in which the gradient chains were radially shifted 1.35 cm further from the reactor core are marked in blue, reference calculations with reference concrete composition are marked in green. The diagrams on the left show the axial profiles of the gradient chains and the diagrams on the right show the relative deviation between different radial positions. The connecting lines serve as an eye guide only. (For interpretation of the references to color in this figure legend, the reader is referred to the web version of this article.)

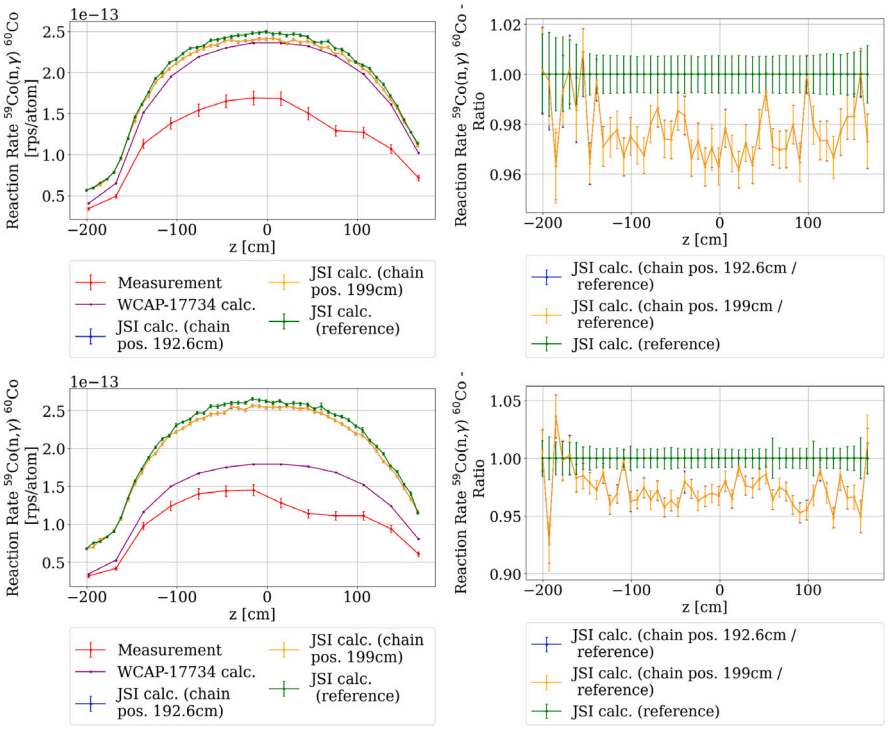

Fig. 39. Measured ^{59}Co(n,γ) reaction rates in gradient chains sensitivity to radial position at location 15° (top) and 30° (bottom). Calculations in which the gradient chains were radially shifted 5.05 cm closer to the reactor core are marked in blue, calculations in which the gradient chains were radially shifted 1.35 cm further from the reactor core are marked in blue, reference calculations with reference concrete composition are marked in green. The diagrams on the left show the axial profiles of the gradient chains and the diagrams on the right show the relative deviation between different radial positions. The connecting lines serve as an eye guide only. (For interpretation of the references to color in this figure legend, the reader is referred to the web version of this article.)

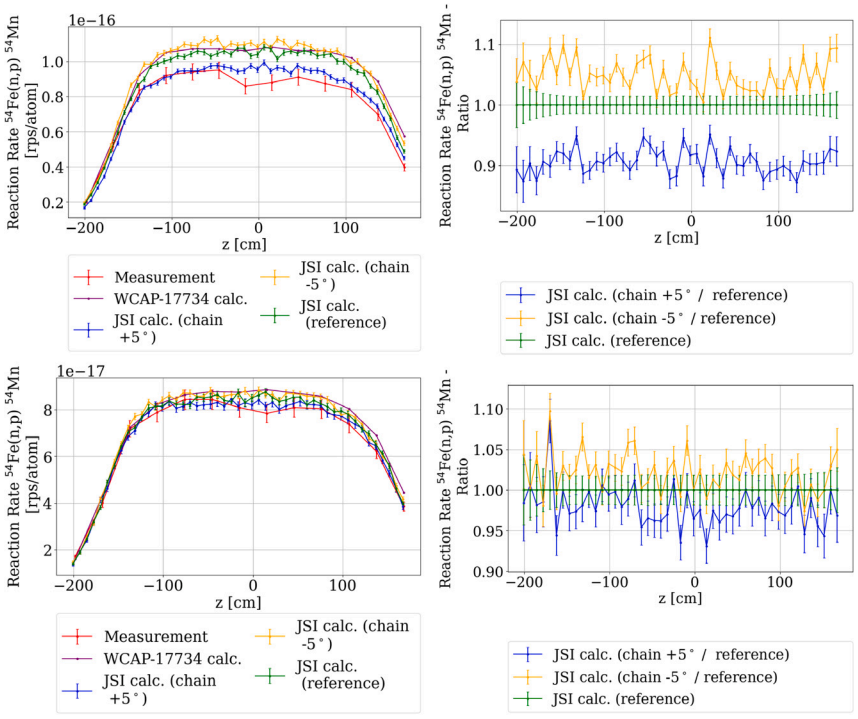

Fig. 40. Measured ^{54}Fe(n,p) reaction rates in gradient chains sensitivity to azimuthal position at location 15° (top) and 30° (bottom). Calculations with an azimuthal shift of +5° are marked in blue, calculations with an azimuthal shift of −5° are marked in orange, reference calculations with the reference chain position are marked in green. The diagrams on the left show the axial profiles of the gradient chain and the diagrams on the right show the relative deviations between the different azimuthal positions. The connecting lines serve as an eye guide only. (For interpretation of the references to color in this figure legend, the reader is referred to the web version of this article.)

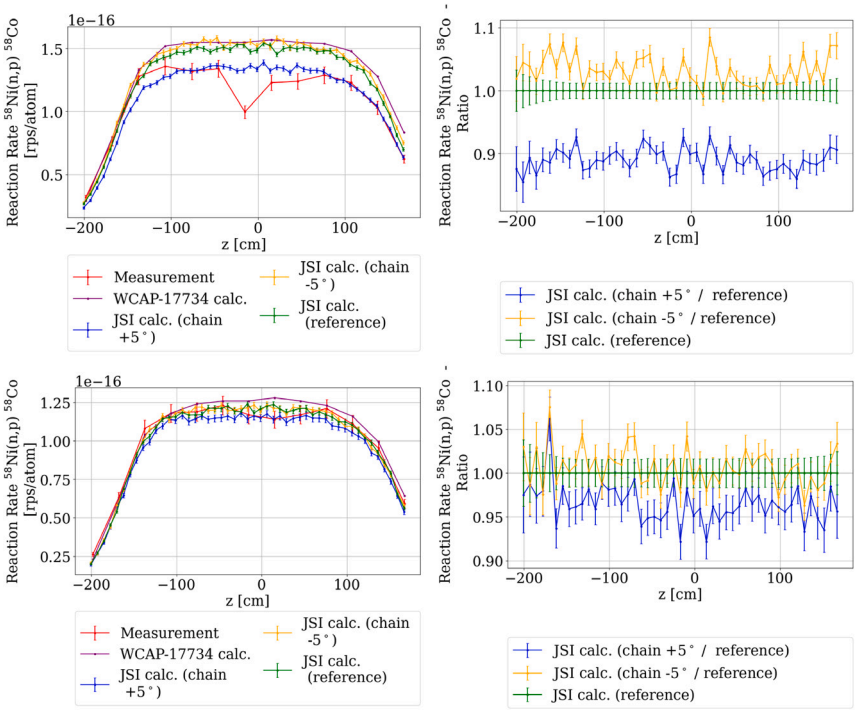

Fig. 41. Measured ^{58}Ni(n,p) reaction rates in gradient chains sensitivity to azimuthal position at location 15° (top) and 30° (bottom). Calculations with an azimuthal shift of +5° are marked in blue, calculations with an azimuthal shift of −5° are marked in orange, reference calculations with the reference chain position are marked in green. The diagrams on the left show the axial profiles of the gradient chain and the diagrams on the right show the relative deviations between the different azimuthal positions. The connecting lines serve as an eye guide only. (For interpretation of the references to color in this figure legend, the reader is referred to the web version of this article.)

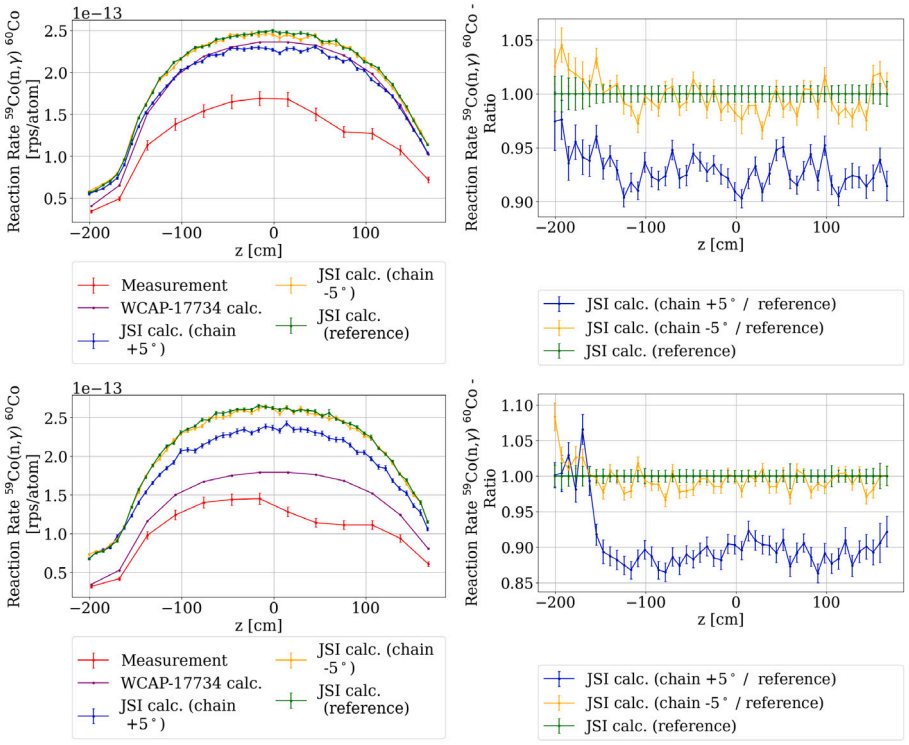

Fig. 42. Measured ^{59}Co(n,γ) reaction rates in gradient chains sensitivity to azimuthal position at location 15° (top) and 30° (bottom). Calculations with an azimuthal shift of +5° are marked in blue, calculations with an azimuthal shift of −5° are marked in orange, reference calculations with the reference chain position are marked in green. The diagrams on the left show the axial profiles of the gradient chain and the diagrams on the right show the relative deviations between the different azimuthal positions. The connecting lines serve as an eye guide only. (For interpretation of the references to color in this figure legend, the reader is referred to the web version of this article.)

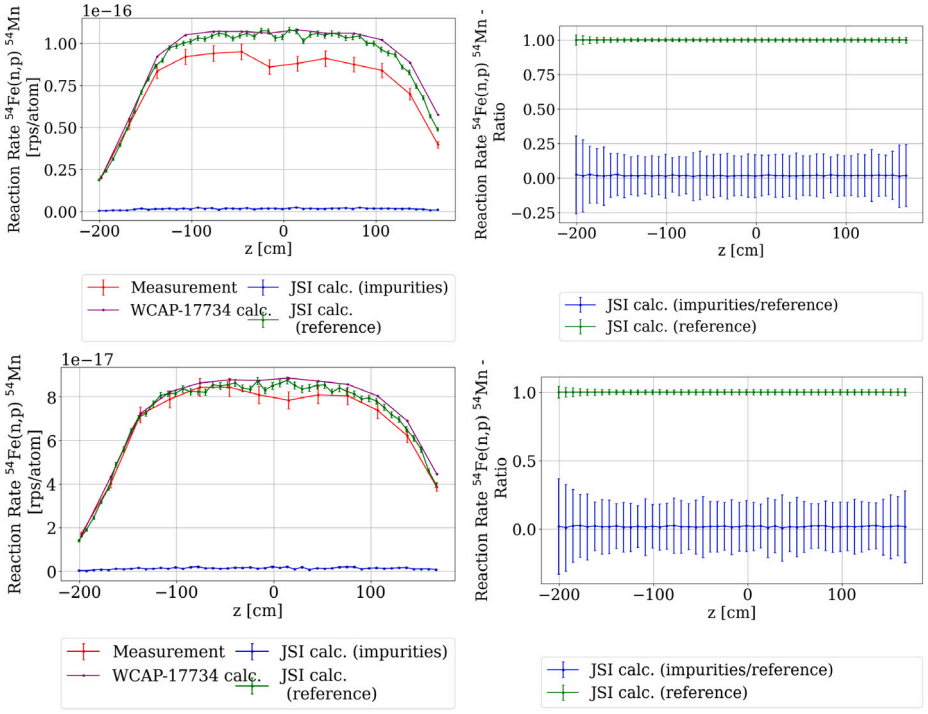

Fig. 43. Measured ^{54}Fe(n,p) reaction rates in gradient chains sensitivity to the presence of impurities in sample at location 15° (top) and 30° (bottom). Calculations for impurities are marked in blue, reference calculations without impurities are marked in green. The diagrams on the left show the axial profiles of the gradient chains and the diagrams on the right show the relative differences in reaction rates. The connecting lines serve as an eye guide only. (For interpretation of the references to color in this figure legend, the reader is referred to the web version of this article.)

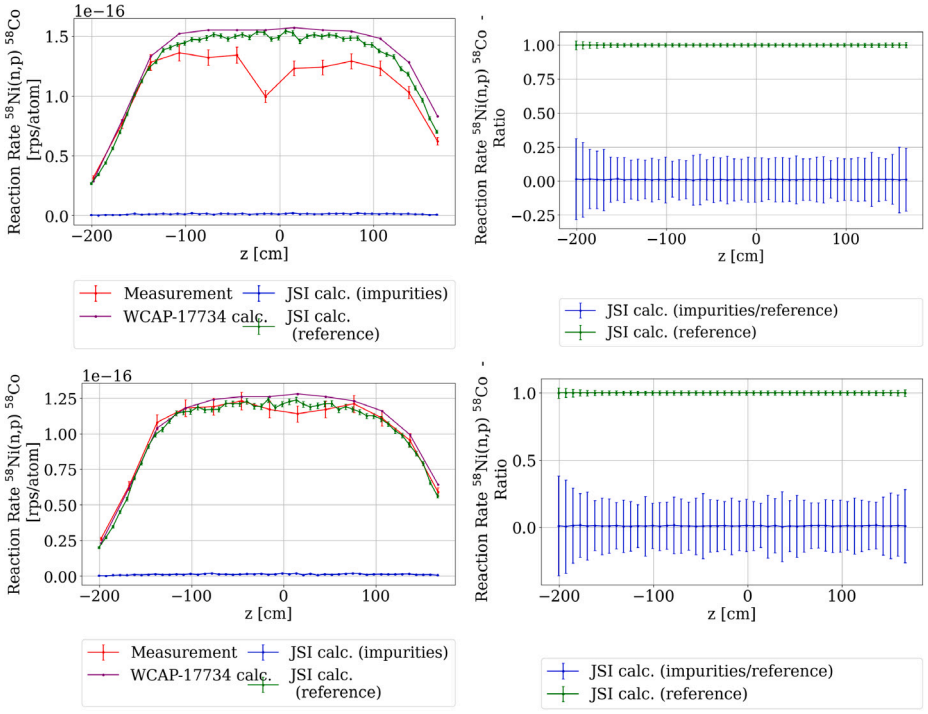

Fig. 44. Measured ^{58}Ni(n,p) reaction rates in gradient chains sensitivity to the presence of impurities in sample at location 15° (top) and 30° (bottom). Calculations for impurities are marked in blue, reference calculations without impurities are marked in green. The diagrams on the left show the axial profiles of the gradient chains and the diagrams on the right show the relative differences in reaction rates. The connecting lines serve as an eye guide only. (For interpretation of the references to color in this figure legend, the reader is referred to the web version of this article.)

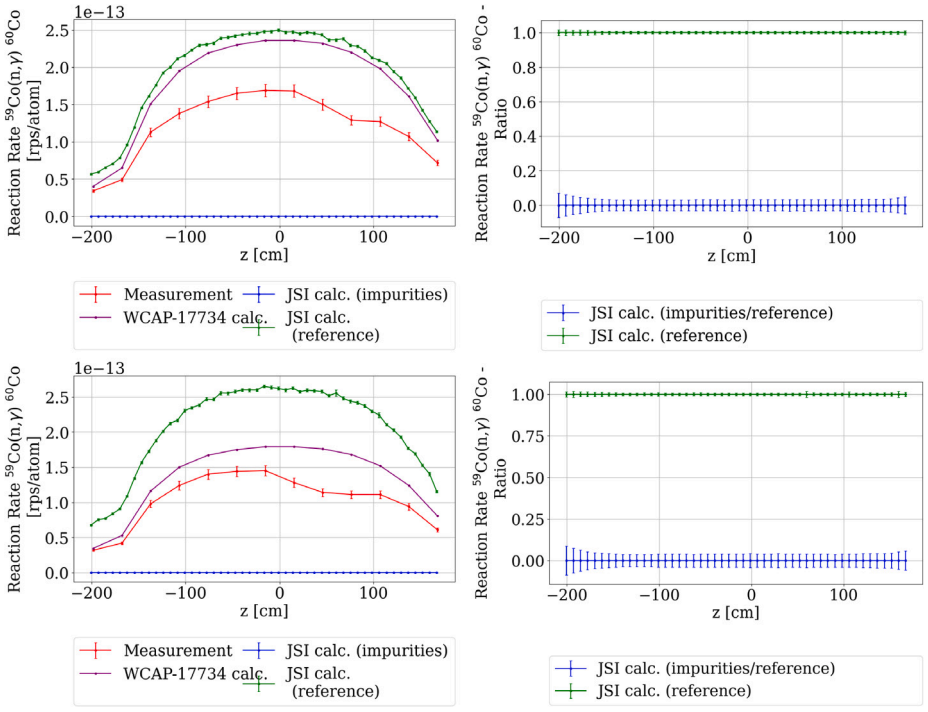

Fig. 45. Measured ^{59}Co(n,γ) reaction rates in gradient chains sensitivity to the presence of impurities in sample at location 15° (top) and 30° (bottom). Calculations for impurities are marked in blue, reference calculations without impurities are marked in green. The diagrams on the left show the axial profiles of the gradient chains and the diagrams on the right show the relative differences in reaction rates. The connecting lines serve as an eye guide only. (For interpretation of the references to color in this figure legend, the reader is referred to the web version of this article.)

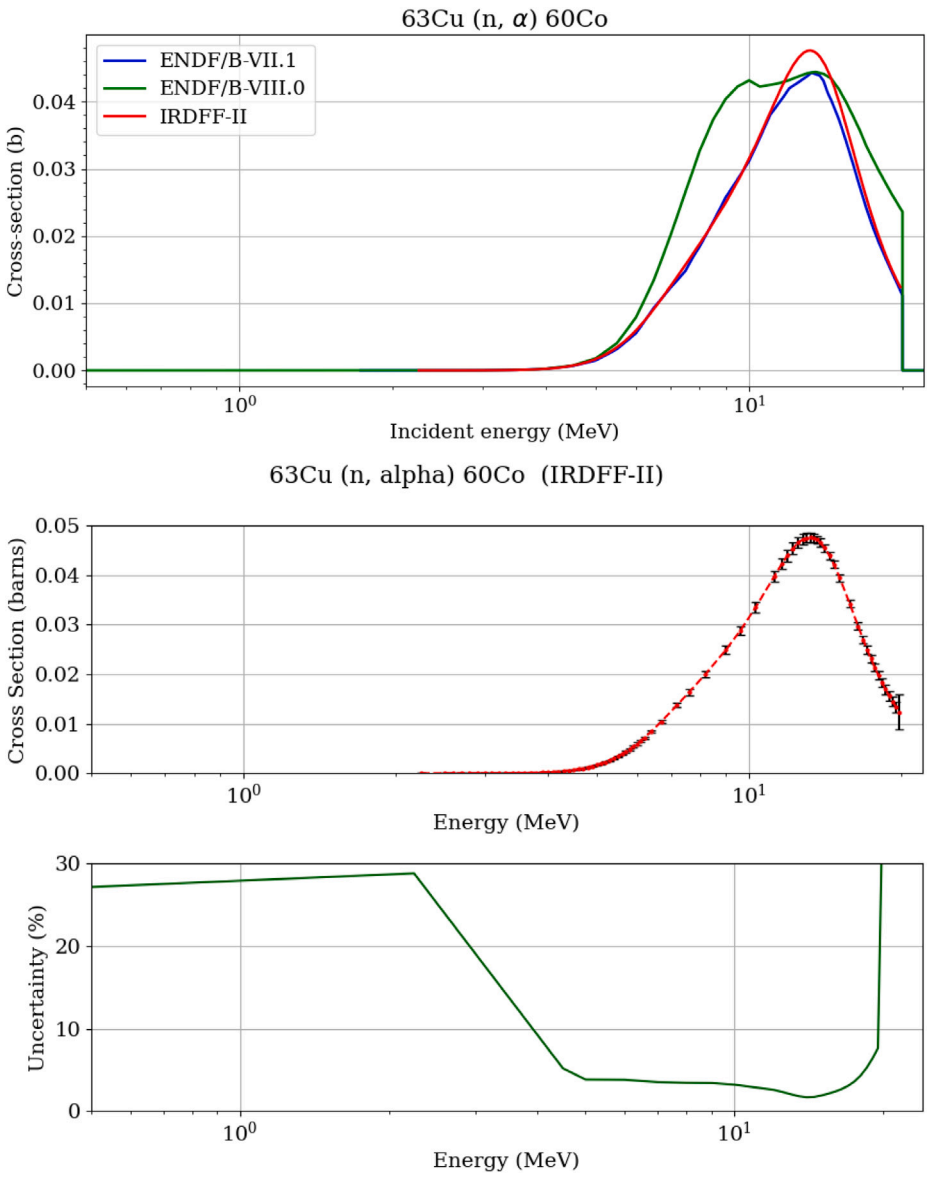

Fig. 46. The top graph shows the reaction cross section for ^{63}Cu(n, α)^{60}Co in different nuclear data libraries (ENDF/B-VIII.0 in black, ENDF/B-VII.0 in green and IRDFF-II in orange). The middle graph shows the reaction cross section in IRDFF-II with uncertainties from the covariance data and the bottom graph shows the uncertainties from the covariance data.

Table 2
Surrounding concrete composition in the current MCNP computational model. In MCNP the atomic fractions for individual material are re-normalized to the sum of 1.

Isotope	Atomic fraction	Isotope	Atomic fraction
^{16}O	4.7383×10^{-2}	^{33}S	4.1091×10^{-7}
^{17}O	1.8049×10^{-5}	^{34}S	2.3285×10^{-6}
^{1}H	1.2344×10^{-2}	^{36}S	5.4788×10^{-9}
^{2}H	1.4198×10^{-6}	^{40}Ca	5.5949×10^{-3}
^{12}C	3.2788×10^{-3}	^{42}Ca	3.7341×10^{-5}
^{24}Mg	5.7094×10^{-5}	^{43}Ca	7.7915×10^{-6}
^{25}Mg	7.2280×10^{-6}	^{44}Ca	1.2039×10^{-4}
^{26}Mg	7.9580×10^{-6}	^{46}Ca	2.3086×10^{-7}
^{27}Al	1.8719×10^{-3}	^{48}Ca	1.0793×10^{-5}
^{28}Si	1.1821×10^{-2}	^{54}Fe	6.8952×10^{-6}
^{29}Si	6.0051×10^{-4}	^{56}Fe	1.0824×10^{-4}
^{30}Si	3.9632×10^{-4}	^{57}Fe	2.4997×10^{-6}
^{32}S	5.2043×10^{-5}	^{58}Fe	3.3267×10^{-7}

5. Conclusion

This study demonstrates the viability and value of high-fidelity Monte Carlo modeling for ex-vessel neutron dosimetry (EVND) in a commercial PWR environment. By applying MCNP in combination with ADVANTG, and using a neutron source term specifically tailored to the 25th fuel cycle of the Krško NPP, we achieved strong agreement between calculated and measured reaction rates across a range of dosimeters and detector locations. The findings validate the approach as a robust tool for plant-specific fluence evaluation.

Beyond validation, the analysis revealed several important factors affecting EVND accuracy. Among them, the backscattering effect from the surrounding concrete had the most pronounced impact on thermal neutron fluence, underscoring the need for accurate material composition and geometric modeling in the ex-core region. Sensitivity studies also showed that while certain uncertainties (e.g., nuclear data or detector position) have a modest effect on fast neutron monitors, thermal neutron reactions are significantly more vulnerable to modeling assumptions and local variations.

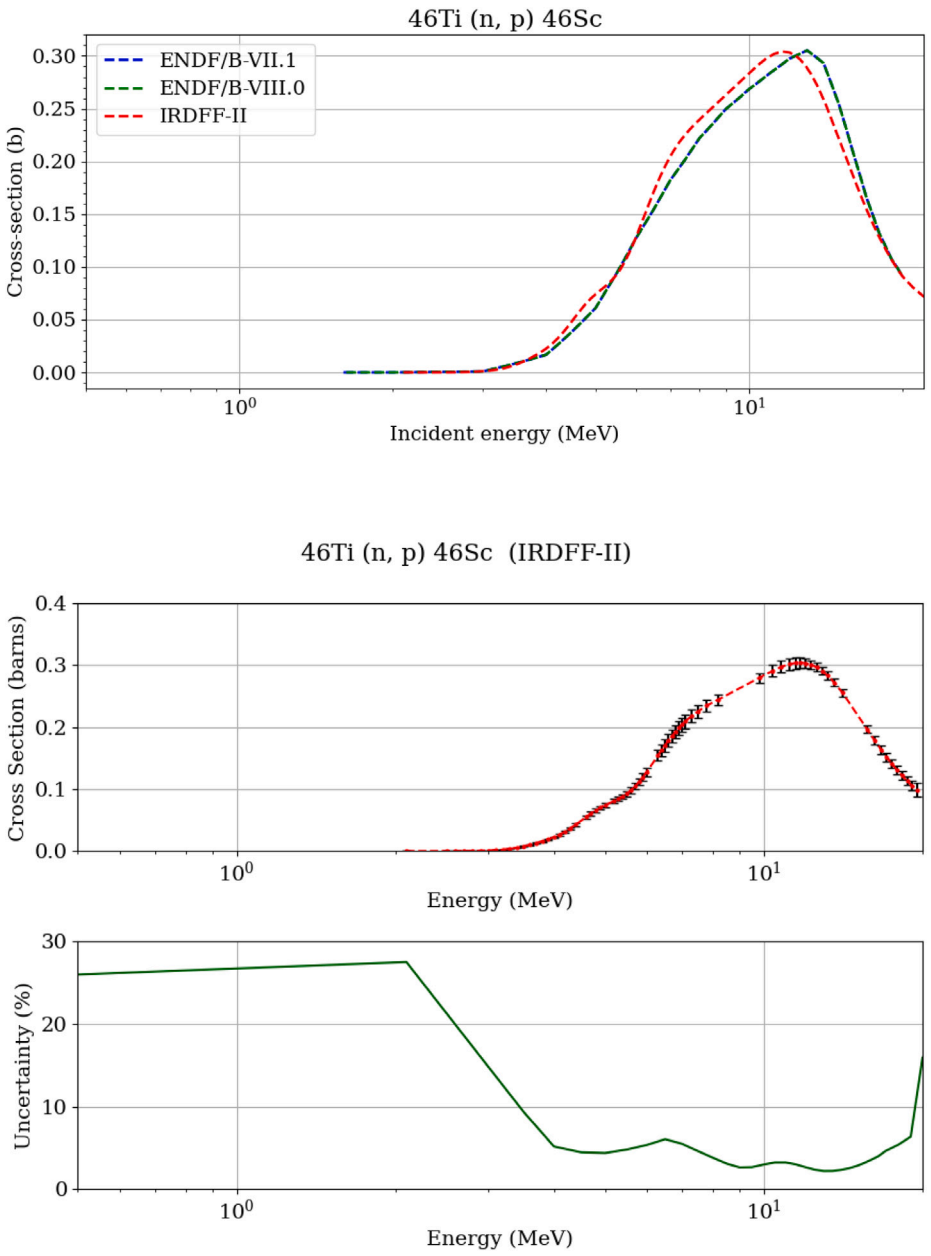

Fig. 47. The top graph shows the reaction cross section for ^{46}Ti(n,p)^{46}Scin different nuclear data libraries (ENDF/B-VIII.0 in black, ENDF/B-VII.0 in green and IRDFF-II in orange). The middle graph shows the reaction cross section in IRDFF-II with uncertainties from the covariance data and the bottom graph shows the uncertainties from the covariance data.

These insights are directly applicable to license renewal, surveillance optimization, and long-term structural integrity monitoring at Krško NPP. More broadly, the approach demonstrated here contributes to a reproducible, physics-based framework for EVND validation using open methods and plant-specific modeling. As more reactors enter extended operation phases, such techniques will be increasingly important in closing the uncertainty gap between simulation and measurement in safety-critical regions of the pressure vessel.

CRediT authorship contribution statement

Tanja Goričanec: Writing – review & editing, Writing – original draft, Validation, Methodology, Investigation, Funding acquisition, Formal analysis, Data curation. **Benjamin Barbarič:** Writing – review & editing, Visualization, Formal analysis. **Vladimir Radulović:** Writing – review & editing. **Dušan Čalič:** Writing – review & editing. **Luka Snoj:** Writing – review & editing, Supervision. **Marjan Kromar:** Writing – review & editing, Supervision, Formal analysis, Conceptualization.

Declaration of competing interest

The authors declare the following financial interests/personal relationships which may be considered as potential competing interests: Tanja Goricanec reports financial support was provided by Slovenian Nuclear Safety Administration. If there are other authors, they declare that they have no known competing financial interests or personal relationships that could have appeared to influence the work reported in this paper.

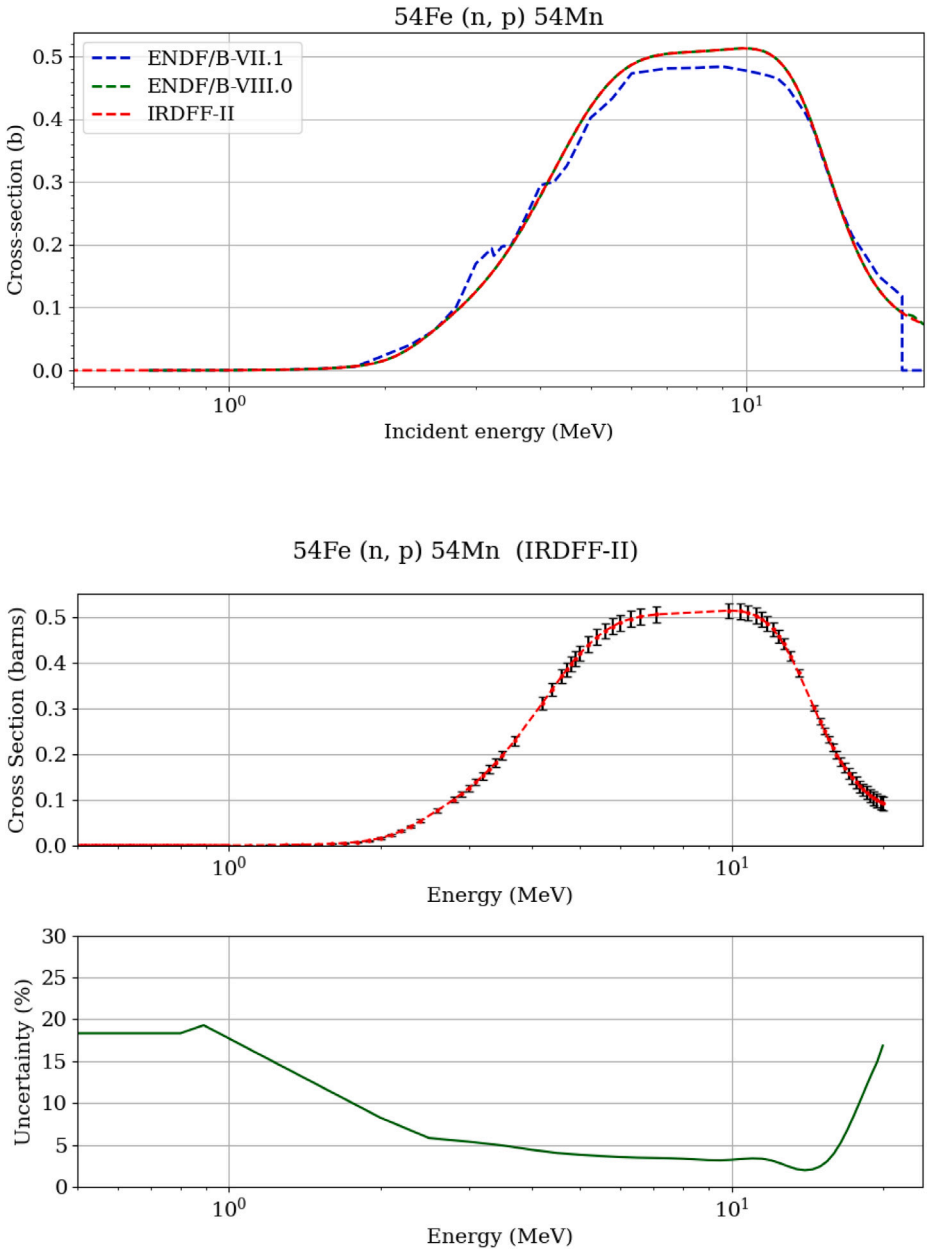

Fig. 48. The top graph shows the reaction cross section for ^{54}Fe(n,p)^{54}Mn in different nuclear data libraries (ENDF/B-VIII.0 in black, ENDF/B-VII.0 in green and IRDFF-II in orange). The middle graph shows the reaction cross section in IRDFF-II with uncertainties from the covariance data and the bottom graph shows the uncertainties from the covariance data.

Acknowledgments

We acknowledge that the research was founded by the project "Izračun transporta nevtronov v zadrževalnem hramu jedrske elektrarne Krško z uporabo Monte Carlo metode" (C2563-24-430012) of the Slovenian Nuclear Safety Administration and by the project "Napredne računske simulacije za analizo nevtronskih poškodb reaktorske posode tlačnovodne jedrske elektrarne" (CRP V2-2531) of the Slovenian Research and Innovation Agency and the Slovenian Nuclear Safety Administration.

Appendix A. Detailed explanation about absolute normalization of MCNP calculation results

For the normalization of the calculation results obtained with MCNP Eq. (1) was used. The reference multiplication factors for the present work were obtained from the eigenvalue core calculation for the 25th fuel cycle of the Krško NPP at the beginning-of-cycle (BOC) and end-of-cycle (EOC). The computed values were:

- BOC: $k_{eff} = 1.00856 \pm 0.00001$
- EOC: $k_{eff} = 1.01091 \pm 0.00002$

The average number of neutrons released during nuclear fission depends on the material in which the fission takes place and the energy spectrum of the neutrons in the reactor core. The number of neutrons released per fission can also be calculated very precisely using the Monte Carlo method:

- BOC: $\overline{\nu} = 2.536$
- EOC: $\overline{\nu} = 2.654$

The determination of the average energy released per fission in MCNP is complex, therefore the approach presented in [32] was

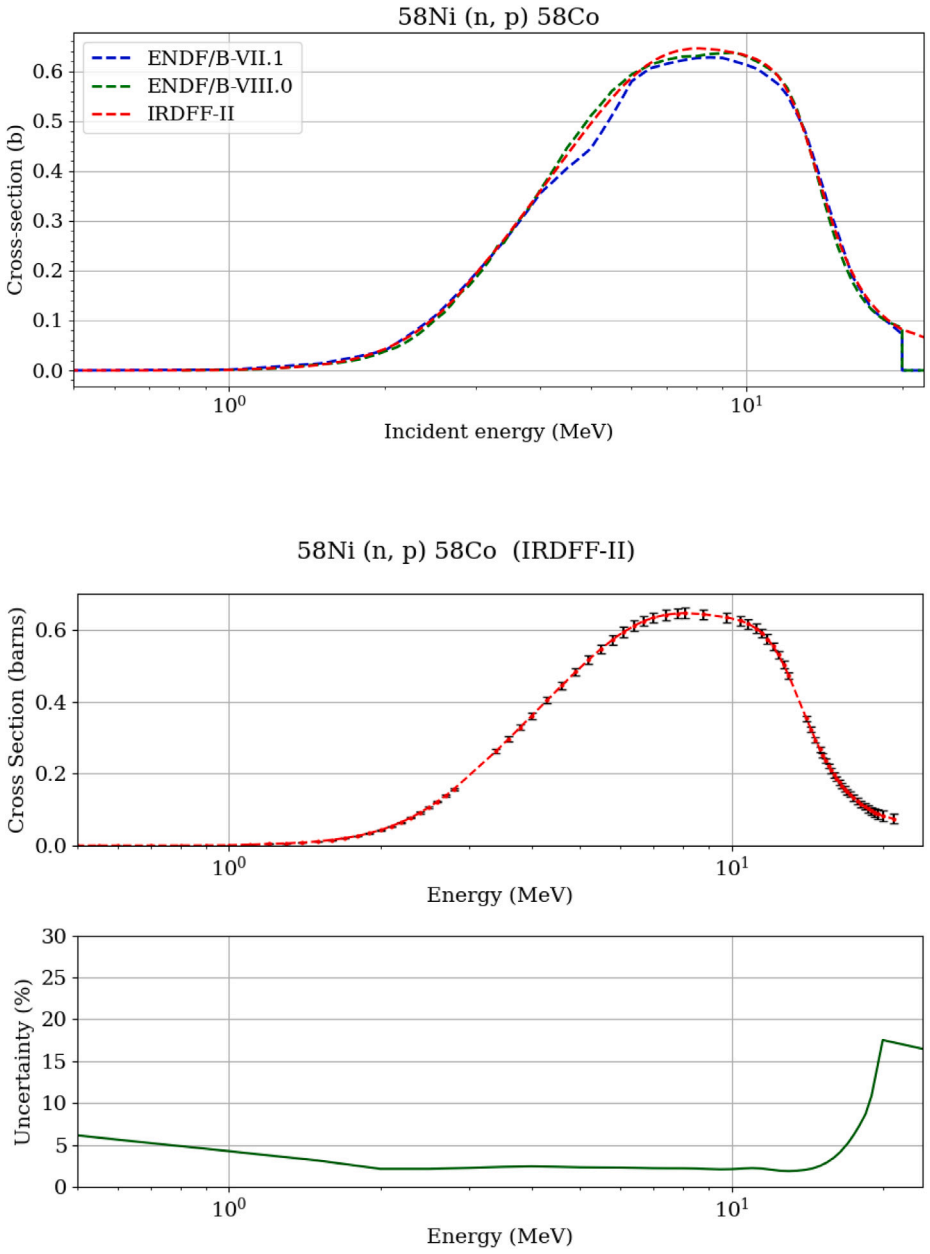

Fig. 49. The top graph shows the reaction cross section for ^{58}Ni(n,p)^{58}Co in different nuclear data libraries (ENDF/B-VIII.0 in black, ENDF/B-VII.0 in green and IRDFF-II in orange). The middle graph shows the reaction cross section in IRDFF-II with uncertainties from the covariance data and the bottom graph shows the uncertainties from the covariance data.

adapted for the first approximation of the energy released per fission. This approach is a first approximation that also takes into account the energies due to capture reactions. It also assumes that all the energy is deposited locally at the fission sites. Since the fuel in typical PWRs, such as the Krško NPP, is partially burned, at least the 4 most important fissile isotopes must be taken into account when calculating the average energy released per fission [21]:

- ^{235}U (Q_{235} = 193.4054 MeV),
- ^{238}U (Q_{238} = 197.7860 MeV)
- ^{239}Pu (Q_{239} = 198.5785 MeV)
- ^{241}Pu (Q_{241} = 201.9801 MeV)

The average energy released per fission can be calculated as follows

$$w_f = \sum n_i E_{fiss,i} = \sum n_i \frac{Q_i}{Q_{235}} H_{235}, \quad (2)$$

where n_i is the relative number of fissions of the individual isotopes compared to the total number of fissions in the reactor core and H_{235} = 202.27 MeV is an estimate for the energy deposition per fission (including the additional energy released in capture reactions) in a typical light water reactor [32]. The average energy released per fission, taking into account Eq. (2), was determined from the eigenvalue Monte Carlo calculation with w_f = 203.9159 MeV for BOC and w_f = 205.2301 MeV for EOC. The relative number of fissions for the most important fissile isotopes is listed in Table A.3.

Appendix B. Supplementary results

In this Appendix are gathered the results supplementing the main results presented in the main part of the paper. Results presenting i.e. different azimuthal positions were not presented in the main part of the paper to help with its readability and consistency.

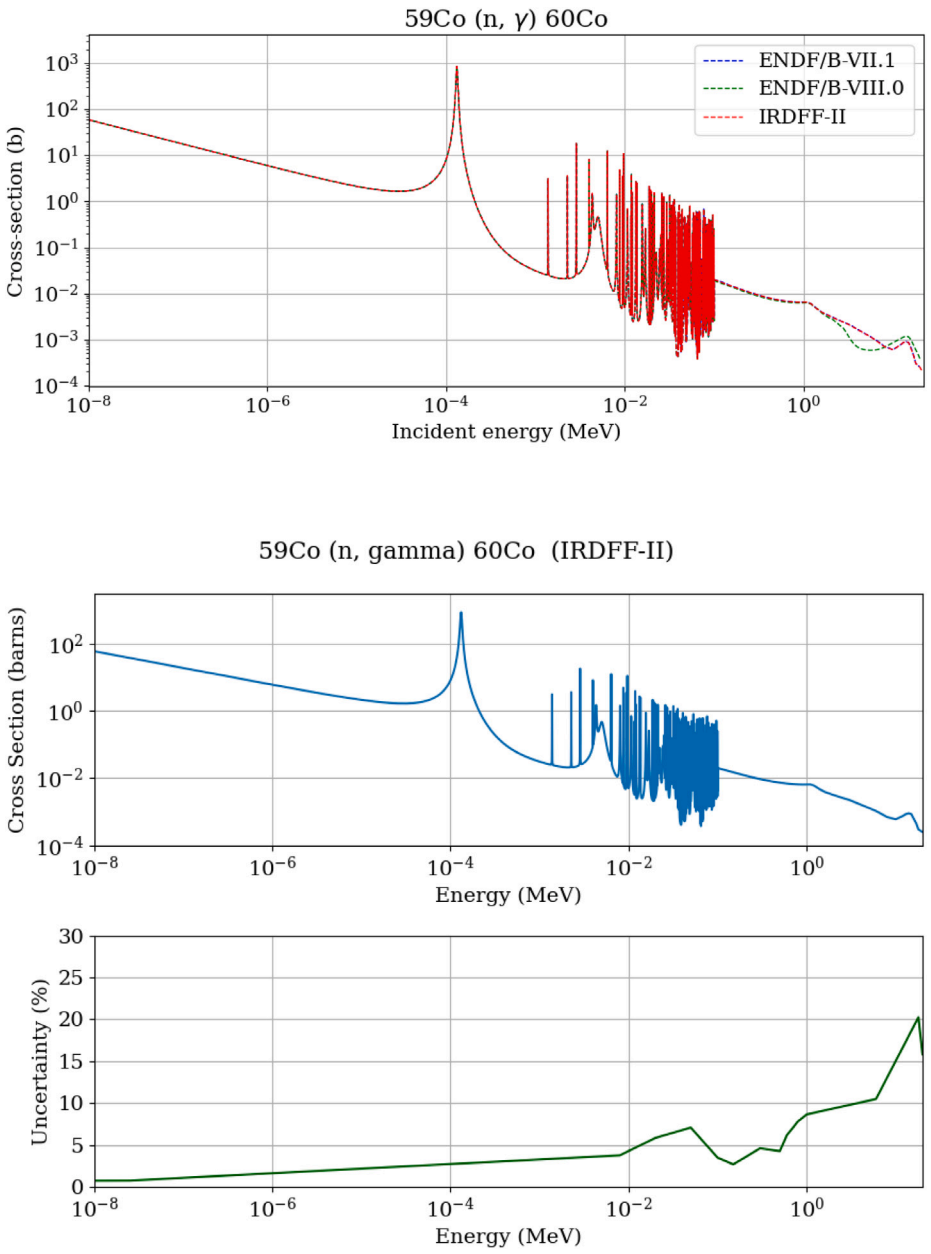

Fig. 50. The top graph shows the reaction cross section for ^{59}Co(n,γ)^{60}Co in different nuclear data libraries (ENDF/B-VIII.0 in black, ENDF/B-VII.0 in green and IRDFF-II in orange). The middle graph shows the reaction cross section in IRDFF-II with uncertainties from the covariance data and the bottom graph shows the uncertainties from the covariance data. (For interpretation of the references to color in this figure legend, the reader is referred to the web version of this article.)

Table A.3
Relative number of fissions per isotope (n_i) for beginning and end of cycle.

Isotope	n_i(BOC)	n_i(EOC)
^{235}U	0.7010	0.4845
^{238}U	0.0833	0.0859
^{239}Pu	0.1883	0.3614
^{241}Pu	0.0274	0.0682

B.1. Supplementary results for reaction rates in gradient chains

In Figs. 21–23 are presented results for all three gradient chains at azimuthal locations 15° and 30° supplementing the results presented in Section 4.1, where reaction rate axial profiles for azimuthal position 0° are presented.

B.2. Supplementary results for EVND capsules

In Tables 4–8 are presented results for all EVND capsules supplementing the results presented in Section 4.2, where comparison of measurements and calculations is presented in plots.

B.3. Supplementary results for sensitivity to nuclear data

In Figs. 25–27 are presented results of sensitivity study on nuclear data for all three gradient chains at azimuthal locations 15° and 30°

Table 4
Measured and calculated reaction rates at core midplane, 0°, Cycle 25. JSI results include both beginning-of-cycle and end-of-cycle core calculations.

Reaction	Measured reaction rate (rps/atom) WCAP-17734	Calculated reaction rate (rps/atom) WCAP-17734	Calculated reaction rate (rps/atom) JSI	M/C ratio WCAP-17734	M/C ratio JSI
$^{63}Cu(n,\alpha)^{60}Co$	1.24×10^{-18} (1 ± 5%)	1.56×10^{-18}	1.55×10^{-18} (1 ± 2.9%)	0.79 (1 ± 14.2%)	0.80 (1 ± 7.3%)
$^{54}Fe(n,p)^{54}Mn$	1.11×10^{-16} (1 ± 5%)	1.46×10^{-16}	1.30×10^{-16} (1 ± 1.2%)	0.76 (1 ± 10.8%)	0.86 (1 ± 6.0%)
$^{58}Ni(n,p)^{58}Co$	1.59×10^{-16} (1 ± 5%)	2.11×10^{-16}	1.86×10^{-16} (1 ± 1.1%)	0.75 (1 ± 10.7%)	0.85 (1 ± 5.4%)
$^{46}Ti(n,p)^{46}Sc$	1.86×10^{-17} (1 ± 5%)	2.29×10^{-17}	2.46×10^{-17} (1 ± 2.1%)	0.81 (1 ± 10.1%)	0.76 (1 ± 6.4%)
$^{93}Nb(n,n')^{93m}Nb$	6.75×10^{-16} (1 ± 5%)	6.92×10^{-16}	5.83×10^{-16} (1 ± 0.4%)	0.98 (1 ± 8.9%)	1.16 (1 ± 5.0%)
$^{59}Co(n,\gamma)^{60}Co$	1.32×10^{-13} (1 ± 5%)	2.79×10^{-13}	3.29×10^{-13} (1 ± 1.0%)	0.47[a]	0.42 (1 ± 5.5%)
$^{59}Co(Cd)(n,\gamma)^{60}Co$	7.15×10^{-14} (1 ± 5%)	1.39×10^{-13}	2.73×10^{-13} (1 ± 1.0%)	0.51[a]	0.81 (1 ± 5.4%)

[a] The uncertainty for reaction were not given in the reference.

Table 5
Measured and calculated reaction rates at core midplane, 15°, Cycle 25. JSI results include both beginning-of-cycle and end-of-cycle core calculations.

Reaction	Measured reaction rate (rps/atom) WCAP-17734	Calculated reaction rate (rps/atom) WCAP-17734	Calculated reaction rate (rps/atom) JSI	M/C ratio WCAP-17734	M/C ratio JSI
$^{63}Cu(n,\alpha)^{60}Co$	9.79×10^{-19} (1 ± 5%)	1.22×10^{-18}	1.36×10^{-18} (1 ± 2.9%)	0.80 (1 ± 14.2%)	0.72 (1 ± 7.3%)
$^{54}Fe(n,p)^{54}Mn$	8.73×10^{-17} (1 ± 5%)	1.12×10^{-16}	1.07×10^{-16} (1 ± 1.3%)	0.78 (1 ± 10.8%)	0.82 (1 ± 6.0%)
$^{58}Ni(n,p)^{58}Co$	1.22×10^{-16} (1 ± 5%)	1.61×10^{-16}	1.53×10^{-16} (1 ± 1.1%)	0.76 (1 ± 10.7%)	0.80 (1 ± 5.4%)
$^{46}Ti(n,p)^{46}Sc$	1.43×10^{-17} (1 ± 5%)	1.77×10^{-17}	2.13×10^{-17} (1 ± 2.1%)	0.81 (1 ± 10.1%)	0.67 (1 ± 6.4%)
$^{93}Nb(n,n')^{93m}Nb$	5.52×10^{-16} (1 ± 5%)	5.43×10^{-16}	4.77×10^{-16} (1 ± 0.4%)	1.02 (1 ± 8.9%)	1.16 (1 ± 5.0%)
$^{59}Co(n,\gamma)^{60}Co$	1.63×10^{-13} (1 ± 5%)	2.38×10^{-13}	3.22×10^{-13} (1 ± 1.0%)	0.71[a]	0.52 (1 ± 5.5%)
$^{59}Co(Cd)(n,\gamma)^{60}Co$	8.04×10^{-14} (1 ± 5%)	1.24×10^{-13}	1.01×10^{-13} (1 ± 1.0%)	0.65[a]	0.80 (1 ± 5.4%)

[a] The uncertainty for reaction were not given in the reference.

supplementing the results presented in Section 4.3.1, where reaction rate axial profiles for azimuthal position 0° are presented.

B.4. Supplementary results for sensitivity to concrete material composition

In Figs. 28–30 are presented results of sensitivity study to concrete material composition for all three gradient chains at azimuthal locations 15° and 30° supplementing the results presented in Section 4.3.2, where reaction rate axial profiles for azimuthal position 0° are presented.

B.5. Supplementary results for sensitivity to concrete geometry

In Figs. 31–33 are presented results of sensitivity study to concrete radius for all three gradient chains at azimuthal locations 15° and 30° supplementing the results presented in Section 4.3.3, where reaction rate axial profiles for azimuthal position 0° are presented.

In Figs. 34–36 are presented results of sensitivity study to possible crack in concrete for all three gradient chains at azimuthal locations 15° and 30° supplementing the results presented in Section 4.3.3, where reaction rate axial profiles for azimuthal position 0° are presented.

Table 6
Measured and calculated reaction rates at core midplane, 30°, Cycle 25. JSI results include both beginning-of-cycle and end-of-cycle core calculations.

Reaction	Measured reaction rate (rps/atom) WCAP-17734	Calculated reaction rate (rps/atom) WCAP-17734	Calculated reaction rate (rps/atom) JSI	M/C ratio WCAP-17734	M/C ratio JSI
$^{63}Cu(n,\alpha)^{60}Co$	9.60×10^{-19} (1 ± 5%)	9.40×10^{-19}	1.10×10^{-18} (1 ± 2.9%)	1.02 (1 ± 14.2%)	0.88 (1 ± 7.3%)
$^{54}Fe(n,p)^{54}Mn$	7.79×10^{-17} (1 ± 5%)	8.36×10^{-17}	8.46×10^{-17} (1 ± 1.3%)	0.93 (1 ± 10.8%)	0.92 (1 ± 6.0%)
$^{58}Ni(n,p)^{58}Co$	1.09×10^{-16} (1 ± 5%)	1.21×10^{-16}	1.20×10^{-16} (1 ± 1.1%)	0.90 (1 ± 10.7%)	0.91 (1 ± 5.4%)
$^{46}Ti(n,p)^{46}Sc$	1.30×10^{-17} (1 ± 5%)	1.35×10^{-17}	1.70×10^{-17} (1 ± 2.1%)	0.96 (1 ± 10.1%)	0.77 (1 ± 6.4%)
$^{93}Nb(n,n')^{93m}Nb$	4.66×10^{-16} (1 ± 5%)	4.06×10^{-16}	3.64×10^{-16} (1 ± 0.4%)	1.15 (1 ± 8.9%)	1.28 (1 ± 5.0%)
$^{59}Co(n,\gamma)^{60}Co$	1.34×10^{-13} (1 ± 5%)	1.92×10^{-13}	2.64×10^{-13} (1 ± 1.0%)	0.70[a]	0.51 (1 ± 5.5%)
$^{59}Co(Cd)(n,\gamma)^{60}Co$	6.80×10^{-14} (1 ± 5%)	1.00×10^{-13}	7.93×10^{-14} (1 ± 1.7%)	0.68[a]	0.86 (1 ± 5.4%)

[a] The uncertainty for reaction were not given in the reference.

Table 7
Measured and calculated reaction rates at core top, 0°, Cycle 25. JSI results include both beginning-of-cycle and end-of-cycle core calculations.

Reaction	Measured reaction rate (rps/atom) WCAP-17734	Calculated reaction rate (rps/atom) WCAP-17734	Calculated reaction rate (rps/atom) JSI	M/C ratio WCAP-17734	M/C ratio JSI
$^{63}Cu(n,\alpha)^{60}Co$	6.15×10^{-19} (1 ± 5%)	8.86×10^{-19}	7.66×10^{-19} (1 ± 4.0%)	0.69 (1 ± 14.2%)	0.80 (1 ± 7.3%)
$^{54}Fe(n,p)^{54}Mn$	5.64×10^{-17} (1 ± 5%)	8.29×10^{-17}	6.62×10^{-17} (1 ± 1.7%)	0.68 (1 ± 10.8%)	0.85 (1 ± 6.0%)
$^{58}Ni(n,p)^{58}Co$	8.94×10^{-16} (1 ± 5%)	1.20×10^{-16}	9.54×10^{-16} (1 ± 1.1%)	0.75 (1 ± 10.7%)	0.94 (1 ± 5.4%)
$^{46}Ti(n,p)^{46}Sc$	1.02×10^{-17} (1 ± 5%)	1.30×10^{-17}	1.24×10^{-17} (1 ± 2.1%)	0.78 (1 ± 10.1%)	0.82 (1 ± 6.4%)
$^{93}Nb(n,n')^{93m}Nb$	3.59×10^{-16} (1 ± 5%)	3.88×10^{-16}	3.14×10^{-16} (1 ± 0.5%)	0.92 (1 ± 8.9%)	1.14 (1 ± 5.0%)
$^{59}Co(n,\gamma)^{60}Co$	5.28×10^{-14} (1 ± 5%)	1.34×10^{-13}	1.57×10^{-13} (1 ± 1.3%)	0.39[a]	0.34 (1 ± 5.5%)
$^{59}Co(Cd)(n,\gamma)^{60}Co$	3.73×10^{-14} (1 ± 5%)	6.78×10^{-14}	4.95×10^{-14} (1 ± 3.0%)	0.55[a]	0.76 (1 ± 5.4%)

[a] The uncertainty for reaction were not given in the reference.

B.6. Supplementary data for the sensitivity to position

In Figs. 37–39 are presented results of sensitivity study to chain radial position for all three gradient chains at azimuthal locations 15° and 30° supplementing the results presented in Section 4.3.4, where reaction rate axial profiles for azimuthal position 0° are presented.

In Figs. 40–42 are presented results of sensitivity study to chain azimuthal position for all three gradient chains at azimuthal locations 15° and 30° supplementing the results presented in Section 4.3.4, where reaction rate axial profiles for azimuthal position 0° are presented.

B.7. Supplementary data for sensitivity to impurities

In Figs. 43–45 are presented results of sensitivity study to chain azimuthal position for all three gradient chains at azimuthal locations 15° and 30° supplementing the results presented in Section 4.3.5, where reaction rate axial profiles for azimuthal position 0° are presented.

Appendix C. Cross sections and uncertainties

In the Appendix, the cross section data for selected neutron reactions is presented, together with the uncertainty from covariance data. Evaluated are reactions applied in the EVND Program during 25th fuel cycle at the Krško NPP (see Figs. 46–50).

Table 8
Measured and calculated reaction rates at core bottom, 0°, Cycle 25. JSI results include both beginning-of-cycle and end-of-cycle core calculations.

Reaction	Measured reaction rate (rps/atom) WCAP-17734	Calculated reaction rate (rps/atom) WCAP-17734	Calculated reaction rate (rps/atom) JSI	M/C ratio WCAP-17734	M/C ratio JSI
$^{63}Cu(n,\alpha)^{60}Co$	4.53×10^{-19} (1 ± 5%)	5.09×10^{-19}	5.24×10^{-19} (1 ± 5.3%)	0.89 (1 ± 14.2%)	0.87 (1 ± 7.3%)
$^{54}Fe(n,p)^{54}Mn$	4.41×10^{-17} (1 ± 5%)	4.62×10^{-17}	4.52×10^{-17} (1 ± 2.5%)	0.95 (1 ± 10.8%)	0.98 (1 ± 6.0%)
$^{58}Ni(n,p)^{58}Co$	6.57×10^{-16} (1 ± 5%)	6.64×10^{-16}	6.47×10^{-16} (1 ± 2.1%)	0.99 (1 ± 10.7%)	1.01 (1 ± 5.4%)
$^{46}Ti(n,p)^{46}Sc$	4.84×10^{-18} (1 ± 5%)	7.42×10^{-18}	8.43×10^{-18} (1 ± 3.9%)	0.65 (1 ± 10.1%)	0.57 (1 ± 6.4%)
$^{93}Nb(n,n')^{93m}Nb$	2.22×10^{-16} (1 ± 5%)	2.11×10^{-16}	1.83×10^{-16} (1 ± 0.7%)	1.06 (1 ± 8.9%)	1.21 (1 ± 5.0%)
$^{59}Co(n,\gamma)^{60}Co$	3.67×10^{-14} (1 ± 5%)	6.51×10^{-14}	1.14×10^{-13} (1 ± 2.1%)	0.56[a]	0.32 (1 ± 5.5%)
$^{59}Co(Cd)(n,\gamma)^{60}Co$	1.92×10^{-14} (1 ± 5%)	3.12×10^{-14}	2.93×10^{-14} (1 ± 4.8%)	0.62[a]	0.66 (1 ± 5.4%)

[a] The uncertainty for reaction were not given in the reference.

References

[1] I.A.E. Agency, Integrity of Reactor Pressure Vessels in Nuclear Power Plants: Assessment of Irradiation Embrittlement Effects in Reactor Pressure Vessel Steels, Text, International Atomic Energy Agency, 2009, pp. 1–144, ISBN: 9789201017093 Publication Title: Integrity of Reactor Pressure Vessels in Nuclear Power Plants: Assessment of Irradiation Embrittlement Effects in Reactor Pressure Vessel Steels.

[2] I.A.E. Agency, Plant Life Management Models for Long Term Operation of Nuclear Power Plants, Text, International Atomic Energy Agency, 2015, pp. 1–134, ISBN: 9789201030146 Publication Title: Plant Life Management Models for Long Term Operation of Nuclear Power Plants.

[3] M.A. Hunter, Ex-Vessel Neutron Dosimetry Program for Krško Cycle 25, Tech. Rep. WCAP-17734-NP, Westinghouse Electric Company LLC, USA.

[4] J. Chen, B. Amiri, J. Geer, Estinghouse fluence methodology uncertainty estimates for reactor vessel internals fast neutron exposure evaluation in subsequent license renewal period, in: EPJ Web of Conferences 308, 03012, ISRD 17, 2024.

[5] W.A. Rhoades, R. Childs, The DORT two-dimensional discrete ordinate transport code, Nucl. Sci. Eng. 99 (1) (1988) 88–89.

[6] J. Chen, F.A. Alpan, G. Fischer, A. Fero, Ex-vessel neutron dosimetry analysis for westinghouse 4-loop XL pressurized water reactor plant using the RadTrackTM code system with the 3D parallel discrete ordinates code RAPTOR-M3G, 2011.

[7] J.T. Goorley, M.R. James, T.E. Booth, F.B. Brown, J.S. Bull, L.J. Cox, J.W. Durkee Jr., J.S. Elson, M.L. Fensin, R.A. Forster III, et al., Initial MCNP6 Release Overview-MCNP6 Version 1.0, Tech. Rep., Los Alamos National Lab. (LANL), Los Alamos, NM (United States), 2013.

[8] A. Haghighat, Monte Carlo Methods for Particle Transport, CRC Press, 2020.

[9] Regulatory Guide 1.190, Calculational and Dosimetry Methods for Determining Pressure Vessel Neutron Fluence, Tech. Rep., U.S. Nuclear Regulatory Commisssion, Office of nuclear regulatory research, 2001.

[10] P. Borodkin, N. Khrennikov, VVER-440 Ex-Core Neutron Transport Calculations by MCNP-5 Code and Comparison with Experiment, Switzerland, 2008.

[11] S. Baier, J. Konheiser, E. Ponitz, Further development, validation and verification of the Monte-Carlo code TRAMO on ex-vessel experiments of the Greifswald NPP, in: EPJ Web of Conferences 308, 02005, ISRD 17, 2024.

[12] S. Bznuni, A. Ugujyan, Assessment of uncertainty in the calculation of neutron fluence on the VVER-440 reactor pressure vessel due to uncertainties in neutron-nuclear interaction cross-sections, J. Contemp. Phys. 59 (2024) 138–143.

[13] R. Vuiart, M. Brovchenko, J. Taforeau, V. Jaiswal, E. Dumonteil, A versatile methodology for reactor pressure vessel aging assessments, Nucl. Sci. Eng. 196 (2022) 455–477.

[14] S.W. Mosher, S.R. Johnson, A.M. Bevill, A.M. Ibrahim, C.R. Daily, T.M. Evans, J.C. Wagner, J.O. Johnson, R.E. Grove, ADVANTG An Automated Variance Reduction Parameter Generator, Rev. 1, Tech. Rep., Oak Ridge National Lab. (ORNL), Oak Ridge, TN (United States), 2015.

[15] T. Goričanec, M. Kromar, A. Kavčič, B. Kos, R. Bizjak, I. Lengar, B. Krajnc, L. Snoj, Analysis of the effect of Krško NPP ex-core detector position on their response, in: Proceedings of 30th International Conference Nuclear Energy for New Europe, Bled, Slovenia, 2021.

[16] T. Goričanec, B. Kos, K. Ambrožič, A. Trkov, L. Snoj, M. Kromar, Determination of neutron flux redistribution factors for a typical pressurized water reactor ex-core measurements using Monte Carlo technique, Front. Energy Res. 11 (2023) URL https://www.frontiersin.org/articles/10.3389/fenrg.2023.1137867.

[17] Y. Lee, Analysis of the VENUS-3 PWR pressure vessel surveillance benchmark using TRIPOLI-4.3 Monte Carlo code, J. ASTM Int. 3 (10) (2006) 1–9, http://dx.doi.org/10.1520/JAI100338, arXiv:https://dl.astm.org/jai/article-pdf/3/10/1/15528/10_1520_jai100338.pdf.

[18] M. Kromar, B. Kurinčič, Validation of the CORD-2 system for the NPP Krško nuclear core design calculations, J. Energy - Energ. 65 (1–2) (2016) 105–115, http://dx.doi.org/10.37798/2016651-2134, URL http://journalofenergy.com/index.php/joe/article/view/134. Number: 1-2.

[19] T. Goričanec, Ž. Štancar, D. Kotnik, L. Snoj, M. Kromar, Applicability of the Krško nuclear power plant core Monte Carlo model for the determination of the neutron source term, Nucl. Eng. Technol. 53 (11) (2021) 3528–3542, Publisher: Elsevier.

[20] K. Ambrožič, B. Kos, A. Jazbec, V. Radulovic, L. Snoj, Characterization of neutron fields in the TRIGA irradiation facilities inside and outside the biological shield, in: 26th International Conference Nuclear Energy for New Europe, Bled, Slovenia, 2017.

[21] D.A. Brown, M. Chadwick, R. Capote, A. Kahler, A. Trkov, M. Herman, A. Sonzogni, Y. Danon, A. Carlson, M. Dunn, et al., ENDF/B-VIII.0: The 8th major release of the nuclear reaction data library with CIELO-project cross sections, new standards and thermal scattering data, Nucl. Data Sheets 148 (2018) 1–142, Publisher: Elsevier.

[22] A. Trkov, P.J. Griffin, S.P. Simakov, L.R. Greenwood, K.I. Zolotarev, R. Capote, D.L. Aldama, V. Chechev, C. Destouches, A.C. Kahler, C. Konno, M. Koštál, M. Majerle, E. Malambu, M. Ohta, V.G. Pronyaev, V. Radulović, S. Sato, M. Schulc, E. Šimečková, I. Vavtar, J. Wagemans, M. White, H. Yashima, IRDFF-II: A new neutron metrology library, Nucl. Data Sheets 163 (2020) 1–108, http://dx.doi.org/10.1016/j.nds.2019.12.001, URL https://www.sciencedirect.com/science/article/pii/S0090375219300687.

[23] T. Goričanec, B. Barbarič, V. Radulovic, D. Čalič, L. Snoj, M. Kromar, Advanced Monte Carlo calculations using MCNP of ex-vessel neutron dosimetry for cycle 25 of Krško nuclear power plant, 2025, http://dx.doi.org/10.5281/zenodo.14887749.

[24] G. Žerovnik, M. Podvratnik, L. Snoj, On normalization of fluxes and reaction rates in MCNP criticality calculations, Ann. Nucl. Energy 63 (2014) 126–128, http://dx.doi.org/10.1016/j.anucene.2013.07.045, URL https://www.sciencedirect.com/science/article/pii/S0306454913004003.

[25] M. Pantelias Garcés, Activation Neutronics for the Swiss Nuclear Power Plants (Ph.D. thesis), ETH Zurich, 2013.

[26] M. Chadwick, M. Herman, P. Obložinský, M. Dunn, Y. Danon, A. Kahler, D. Smith, B. Pritychenko, G. Arbanas, R. Arcilla, R. Brewer, D. Brown, R. Capote, A. Carlson, Y. Cho, H. Derrien, K. Guber, G. Hale, S. Hoblit, S. Holloway, T. Johnson, T. Kawano, B. Kiedrowski, H. Kim, S. Kunieda, N. Larson, L. Leal, J. Lestone, R. Little, E. McCutchan, R. MacFarlane, M. MacInnes, C. Mattoon, R. McKnight, S. Mughabghab, G. Nobre, G. Palmiotti, A. Palumbo, M. Pigni, V. Pronyaev, R. Sayer, A. Sonzogni, N. Summers, P. Talou, I. Thompson, A. Trkov, R. Vogt, S. van der Marck, A. Wallner, M. White, D. Wiarda, P. Young, ENDF/B-VII.1 nuclear data for science and technology: Cross sections, covariances, fission product yields and decay data, Nucl. Data Sheets 112 (12) (2011) 2887–2996, http://dx.doi.org/10.1016/j.nds.2011.11.002, URL https://www.sciencedirect.com/science/article/pii/S009037521100113X. Special Issue on ENDF/B-VII.1 Library.

[27] A. Trkov, RR_UNC. URL https://www-nds.iaea.org/IRDFF/rr_unc.for.

[28] J.A. Kulesza, Krško Ex-Vessel Neutron Dosimetry As-Installed Report, Tech. Rep. WCAP-17232-P, Revision 1, Westinghouse Electric Company LLC, USA, 2012.
[29] J.C. Sublet, J. Eastwood, J. Morgan, M. Gilbert, M. Fleming, W. Arter, FISPACT-II; an advanced simulation system for activation, transmutation and material modelling, Nucl. Data Sheets 139 (2017) 77–137.
[30] B. Barbarič, Aktivacija Komponent Sredice Jedrske Elektrarne Krško, in: Magistrsko Delo, Univerza v Ljubljani, Fakulteta za matematiko in fiziko, 2024.
[31] M. Kromar, Core Follow Analysis and Operational Support - Cycle 25, IJS Delovno Poročilo, Inštitut Jožef Stefan, 2012.
[32] R. Tuominen, V. Valtavirta, J. Leppänen, New energy deposition treatment in the serpent 2 Monte Carlo transport code, Ann. Nucl. Energy 129 (2019).